Methane Hydrate Formation on Clay Mineral Surfaces: Thermodynamic Stability and Heterogeneous Nucleation Mechanisms

Stephanie L. Teich-McGoldrick, David B. Hart, Margaret E. Gordon, Stephen P. Meserole, Mark A. Rodriguez, Konrad Thürmer, Randall T. Cygan, Chunqing Yuan, Greg A. Kimmel, Bruce D. Kay, and R. Scott Smith

Sandia National Laboratories

Methane Hydrate Formation on Clay Mineral Surfaces: Thermodynamic Stability and Heterogeneous Nucleation Mechanisms

Stephanie L. Teich-McGoldrick, David B. Hart
Geochemistry Department

Margaret E. Gordon
Materials, Devices, and Energy Technologies

Stephen P. Meserole
Electronic, Optical, and Nano Materials Department

Mark A. Rodriguez
Materials Characterization and Performance Department

Konrad Thürmer
Materials Physics Department

Randall T. Cygan
Geoscience Research and Applications Group
Sandia National Laboratories
P.O. Box 5800
Albuquerque, New Mexico 87185-MS0754

Chunqing Yuan, Greg A. Kimmel, Bruce D. Kay, and R. Scott Smith
Fundamental and Computational Sciences Directorate
Pacific Northwest National Laboratory
P.O. Box 999
Richland, Washington 99352

Abstract

Heterogeneous nucleation of methane hydrates has been examined using molecular simulation, experimental bulk synthesis, and scanning probe microscopy. Theoretical nucleation rates were determined using molecular dynamics simulations as a function of clay surface represented by hydrophobic and hydrophilic systems. Methane hydrates were synthesized with and without Na-montmorillonite in a bulk reactor pressure assembly. X-ray diffraction and Raman spectroscopy confirm the nucleation and growth of the synthesized hydrates. Various kinetic pathways were explored to produce methane or isobutene clathrates in an ultra-high vacuum apparatus at very low temperatures but scanning probe microscopy only indicates the formation of ice.

ACKNOWLEDGMENTS

CONTENTS

Figures

Tables

1. INTRODUCTION

1.1. Methane Hydrates in Energy and Climate

Methane hydrates, ice-like water cages surrounding methane molecules, play a critical role in our nation's energy resources, energy security, and global climate change. However, the nucleation and growth mechanisms of hydrates and their thermodynamic stability on natural surfaces remain unknown. Accordingly, this project has examined the links between molecular processes and macroscopic behavior of methane hydrate materials based on nucleation and growth phenomena. Using molecular simulation, bulk synthesis, analytical characterization, and scanning probe microscopy, we have developed a foundation for a comprehensive molecular-level understanding of the heterogeneous nucleation mechanism of methane hydrates.

The fundamental structure of methane hydrate is the water cage created by the hydrogen bonding of water molecules surrounding a guest molecule (e.g., methane). Various configurations of cages—also referred to as clathrates—can coordinate to produce a long-range ordered crystalline hydrate with methane distributed among the different-sized cages. Structure I is the most common methane hydrate in nature (Figure 1-1).
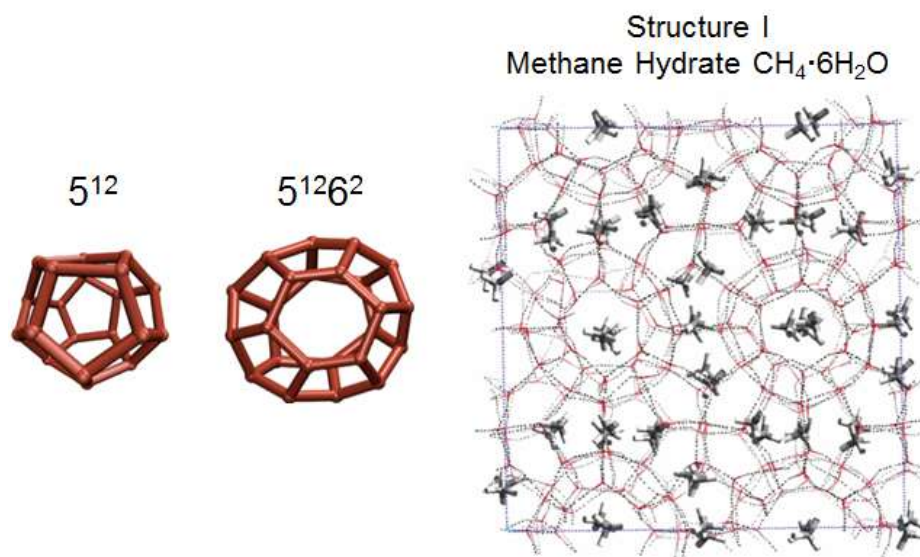
Figure 1-1. Two basic cage structures of water, as defined by oxygen linkages, where pentagonal 5^n and hexagonal 6^n rings are combined to create each cage (left), and a snapshot from a molecular dynamics simulation of Structure I methane hydrate with hydrogen bonds depicted between hydrogen and oxygen atoms of different water molecules (right). Methane guest molecules occupy the water cages.

Large quantities of untapped natural gas exist as hydrates in the Arctic tundra and seabed where clay minerals compose a significant fraction of the sediments. Conversely, as seen in the Gulf of Mexico oil disaster in 2010, gas hydrates can plug crude oil pipelines leading to flow assurance problems, considerable cost, and significant safety and environmental hazards. Additionally,

greenhouse gas sequestration in hydrates could provide a partial solution to global climate change, especially if the hydrate formation rate could be enhanced by natural surfaces because methane is twenty times more effective, in the short term, than carbon dioxide in trapping heat in the atmosphere. Decomposition of methane hydrates by increasing global temperatures due to climate change can potentially lead to a positive feedback mechanism with significant release of methane to the atmosphere.

This project provides a comprehensive understanding of the heterogeneous nucleation of methane hydrates and their associated thermodynamic properties. These results can potentially provide more effective methods to extract subsurface methane (natural gas) from hydrates, and better control hydrate formation associated with oil extraction (pipeline flow assurance). Methane hydrates have the potential to play a huge rule in our nation's energy security. Large untapped hydrate reserves exist in seafloor and Arctic sediments. A recent U.S. Geological survey estimates 590 trillion cubic feet of methane hydrate—more than three times the amount of natural gas—is located on the North Slope of Alaska. The ability to utilize and control hydrate reserves is currently hindered by a lack of fundamental understanding of the natural environment's impact on the stability and formation of methane hydrates, which are often found in areas of clay-rich sediments. Most studies to date on hydrate nucleation and thermodynamic stability have focused on homogeneous systems whereas heterogeneous systems are found in nature and in technical settings. The addition of nucleating mineral surfaces will impact the outcome of any study performed, and will advance this field towards an improved knowledge base furthering our ability to utilize hydrate-based fuel resources.

1.2. Journal Articles Associated with Project

The subsequent sections of this report address the technical tasks associated with the project and provide analytical, experimental, and computational details of the stability of methane hydrates and the role of clay mineral surfaces in the nucleation of methane hydrates. The following list of manuscripts associated with this project have been prepared, submitted to a journal and are in technical review, or have already been published.

Teich-McGoldrick, S.L., Gordon, M.E., and Cygan, R.T. (2015) Effects of water potential on structure and dynamics at the clay surface at ambient conditions. *Journal of Physical Chemistry C*, in prep.

Teich-McGoldrick, S.L., Gordon, M.E., and Cygan, R.T. (2015) Methane hydrate formation in heterogeneous natural environments. *Journal of Physical Chemistry C*, in prep.

Gordon, M.E., Teich-McGoldrick, S.L., Cygan, R.T., Meserole, S.P., and Rodriguez, M.A. (2015) Surface-assisted formation of methane hydrates on ice and Na-montmorillonite clay. *Chemical Engineering Science*, submitted.

Thürmer, K., Yuan, C., Kimmel, G.A., Kay, B.D., and Smith, R.S. (2015) Weak interactions between water and clathrate-forming gases at low pressures. *Surface Science*, 641, 216-223.

2. ROLE OF WATER MODELS IN MOLECULAR-LEVEL STRUCTURING AND DYNAMICS AT THE SURFACE OF CLAY MINERALS

2.1. Introduction

Clay minerals are an important class of natural materials found throughout the Earth's surface. Many critical geochemical phenomena occur at the clay mineral-water interface, including adsorption-desorption processes, transport, nucleation, chemical reactions, and dissolution, which impact a variety of applications including engineered barriers, contaminant transport in the environment, fossil energy extraction, and underground carbon dioxide sequestration. The type of clay mineral present can substantially influence the hydrogen bonding network of interfacial water, and therefore lead to variations in the structure and dynamics of both the water and solutes. Characteristic time scales (femtoseconds to nanoseconds) and length scales (Ångstroms to nanometers) associated with these processes can be effectively probed using molecular simulation techniques.

To understand the structure and dynamics of water over natural surfaces using molecular simulation, compatible force fields are needed. One of the most widely used clay potential is the Clayff potential of Cygan et al (2004). This potential provides a non-bonded flexible description of hydrated clay-mineral systems through the combination of Lennard-Jones (LJ) parameters, harmonic bond and angel terms, and electrostatic point charges derived from quantum calculations. Clayff was developed using the flexible SPC water model to describe system water and clay mineral hydroxyl groups. Specifically, the choice of water model was made to capture the transfer of vibrational energy between the clay-mineral and fluid interface. However, the flexible SPC model of water is not the only water model available for use.

As water is of critical importance in nature, a large amount of scientific effort is focused on correctly characterizing water molecular interactions. Empirical water models are parameterized to capture bulk thermodynamic properties, and the choice of water model is driven by the specific property being probed. While the flexible SPC water potential used as a basis for Clayff has been very successful in the study of geologic interfaces, there are reasons for selecting a different water model. For example, TIP3P is a popular water force field that is often the compatible force field for modeling biomolecules. The rigid SPC model can be selected over the flexible SPC model to match the oxygen and hydrogen LJ parameters of Clayff but gain computational speed-ups. TIP4P was proposed by Jorgensen et al. (1983). The TIP4P-Ice model was parameterized by Vega et al. (2005) in an effort to overcome the lack of accurate prediction of the liquid-solid phase equilibrium of water. The ability of simulations to accurately describe natural phenomena is linked to the accuracy and compatibility of force fields.

The present study investigates the influence of water potential on water structuring and dynamics at a clay mineral surface described by the Clayff force field. We focus our study on the (001) basal surface of two common clay minerals—montmorillonite and kaolinite—in contact with water described by some of the most widely used water potentials (SPC-Rigid, TIP3P, TIP4, TIP4P-Ice, and SPC-Flexible). In neglecting polarizability and quantum effects, all of these models simplify actual water intermolecular interactions. However, the trade-off of computational speed has allowed for many successful studies of both bulk water and interfacial

water. The choice of clay minerals was made to include a phase with associated surface cations (montmorillonite) and hydroxylated and non-hydroxylated surfaces (kaolinite). After describing the simulation models and methods, we compare the structural and diffusion properties of water at a surface as a function of water model.

2.2.   Molecular Models

We examine two natural surfaces in this study—montmorillonite and kaolinite (Figure 2-1 and Figure 2-2). Montmorillonite is a smectite clay with a layered structure comprised of tetrahedral (T) silicate layers and octahedral (O) alumina layers joined through the sharing of oxygen atoms to form a TOT structure. Magnesium (Mg^{2+}) is substituted for aluminum (Al^{3+}) creating a negative charge that is compensated by interlayer sodium cations. The monoclinic unit cell formula is $NaSi_8Al_3MgO_{20}(OH)_4$. The montmorillonite unit cell was expanded to 10 x 6 x 2 in the a, b, and c directions, respectively, to produce a starting structure with dimensions 5.16 nm x 5.38 nm x 1.87 nm. Kaolinite $Al_2Si_2O_5(OH)_4$ is a layered aluminosilicate phase composed of a tetrahedral silicate bonded to an octahedral alumina sheet through shared oxygen atoms. This layering forms a TO structure with two distinct surfaces that form on the (001) basal cleavage plane: an aluminum hydroxide surface and a siloxane surface. There are no atomic substitutions in the kaolinite model and, therefore, there are no charge balancing counter ions associated with the structure. The triclinic crystal structure for kaolinite is taken from the work of Bish et al. (1993) and the experimental unit cell parameters $a = 5.1535$ Å, $b = 8.9419$ Å, $c = 7.3906$ Å, $\alpha = 91.926°$, $\beta = 105.046°$, $\gamma = 89.797°$ are reproduced in our simulation work. The kaolinite substrate is generated by replicating the unit cell 10 x 6 x 2 to produce a starting structure with dimensions 5.15 nm x 5.37 nm x 1.43 nm. Systems consisted of 6400 water molecules in contact with the basal surface of either montmorillonite or kaolinite at ambient conditions $T = 298$ K and $P = 1$ bar. This results in sufficient water depth above the clay surface to achieve bulk properties. The montmorillonite and kaolinite crystal structures are modeled using the Clayff force field (Cygan et al., 2004). In this study, we do not include the three-body angle bend term to describe the surface hydroxyls.
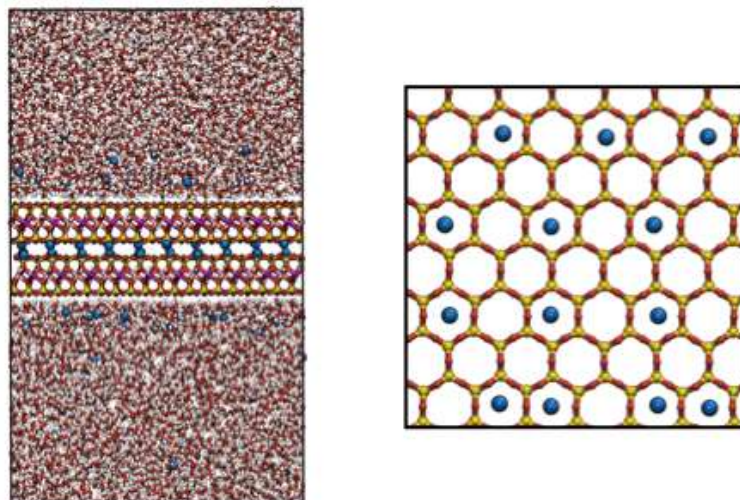
Figure 2-1. Molecular dynamics snapshot of montmorillonite and water model (*xz* plane) (left). Image of the basal surface of montmorillonite illustrating the siloxane rings and associated sodium ions (right). Atoms are colored purple for magnesium, blue for sodium, yellow for silicon, red for oxygen, white for hydrogen, and pink for aluminum.
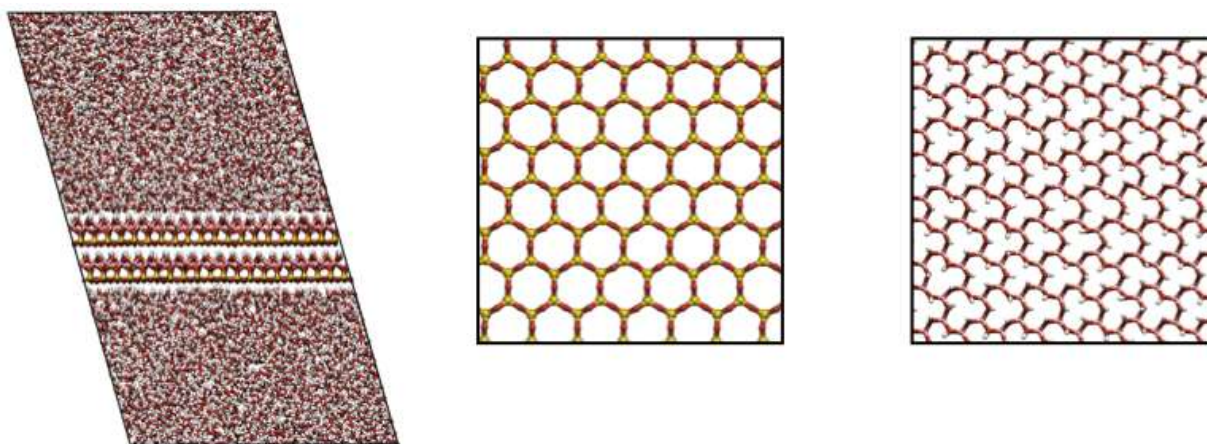
Figure 2-2. Molecular dynamics snapshot of kaolinite and water model (*xz* plane) (left). Image of the kaolinite siloxane surface (hydrophobic) (center). Image of the kaolinite gibbsite surface (hydrophilic) (right). Atoms are colored yellow for silicon, red for oxygen, white for hydrogen, and pink for aluminum.

Clayff force field was developed for use with the modified SPC water potential of Teleman et al. (1987) allowing full flexibility of the water molecule. In addition to this modified SPC water model, simulations were performed using the Tip4P-Ice, the rigid SPC water model, and the TIP3P water model (Figure 2-3). Water models are parameterized to match bulk experimental properties including fluid density, enthalpy, vapor-liquid equilibrium curves, thermodynamic phase boundaries, and dielectric constants. We probe only non-polarizable water models and all of them are rigid expect for the SPC-flexible model associated with Clayff. These water models

represent a variety of differences in geometry, charge, and charge distributions. The bond geometry for the TIP3P, TIP4P, and TIP4P-Ice models have a smaller bond angle and a shorter bond distance as compared to the SPC models. Additionally, while in every model the positive charge is placed on the hydrogen atom, the location of the negative charge associated with the oxygen varies from being directly on the oxygen atom to being located directly below the oxygen on a dummy atom. Each water model has been parameterized to reproduce a different target property.
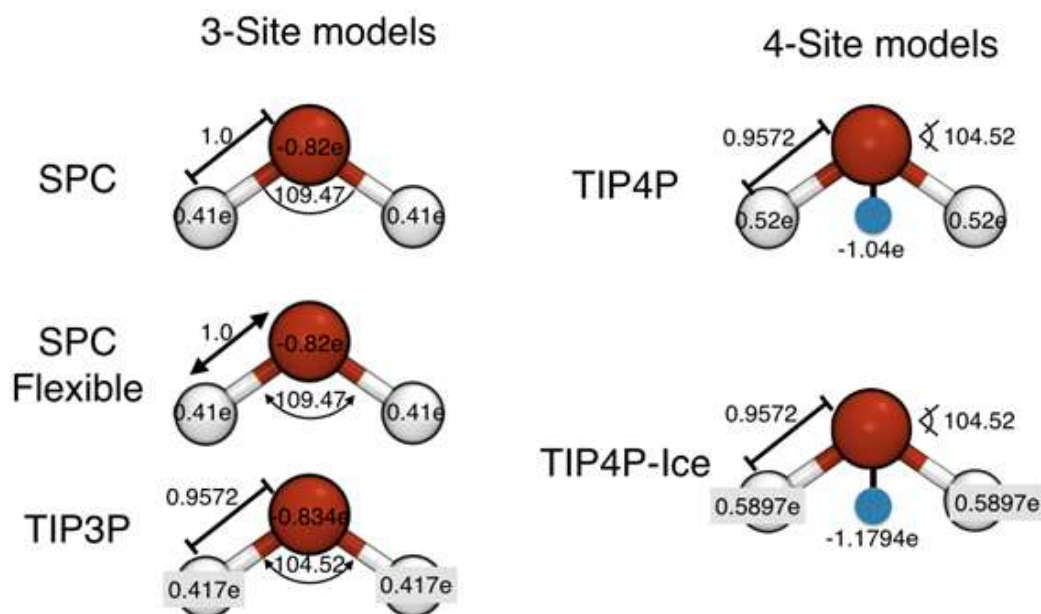
Figure 2-3. Schematic representaiton of the five water models are investigated in this study. The geometry, charge, and charge location varies between the different water models.

2.3. Methods

Atomistic phenomena can be studied using molecular dynamics and can often probe spatial and temporal scales that are inaccessible to experiments. Molecular dynamic (MD) simulations are started with a random configuration of particles (Figure 2-4). Intermolecular interactions define the potential energy between atoms as a function of the distance between atoms. As the simulation progresses, atomic velocities and positions are updated using by solving Newton's equations of motion. System properties are calculated from averages of particle positions and velocities.

MD simulations were performed using the GROMACS simulation package (Berendsen et al. 1995), with a leap-frog integrator used to integrate Newton's equations of motion. A time step of 2 fs was used for all systems except for those using flexible waters in which a time step of 0.2 fs was used. Simulations were equilibrated in the *NPT* ensemble before production runs were conducted in the *NVT* ensemble. In the former, pressure was controlled using an anisotropic Parrinello-Rahman barostat with a time constant of 4 ps and a compressibility of 4.5 x 10^{-5}. In

both equilibration and production runs, temperature was controlled using the Nose-Hoover thermostat with a time constant of 2 ps. Full periodic boundary conditions were applied. A cutoff of 10 nm was used for short-range interactions. Long-range electrostatic interactions were modeled with a particle-mesh Ewald method using a Fourier grid spacing of 0.12 nm. Lorentz-Berthelot mixing rules were employed. The SETTLE algorithm is used to model rigid water models. In simulations with rigid water models, the clay hydroxyl bond lengths are held constant as well. Structural properties were computed from data collected every 5 ps over a 5 ns simulation, while dynamic properties were computed by averaging values from three simulations in which data was collected every 0.05 ps over 0.5ns.
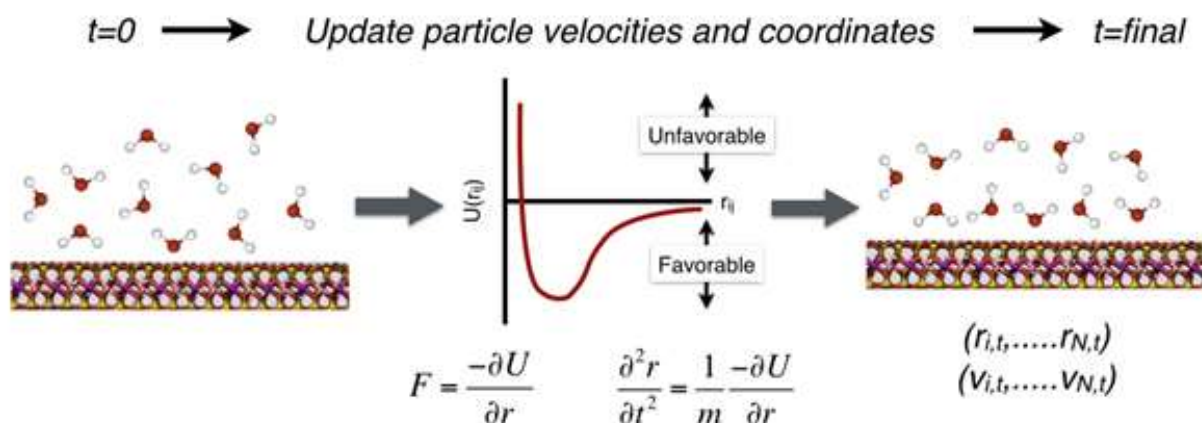
Figure 2-4. Graphical representation of molecular dynamics simulation. Simulations are started from approximate and random atomic configurations. Atomic positions and velocities are updated throughout the simulation until a final equilibrated configuration is reached.

2.4. Results and Discussion

2.4.1. Structural properties

2.4.1.1. Atomic density profiles

The one-dimensional density profiles for water oxygen atoms at the basal surface of kaolinite and montmorillonite are shown in Figure 2-5. Locations of the surface oxygen atoms are at zero distance. The water profiles for each of the five water models are similar over the montmorillonite and kaolinite siloxane surfaces. For the montmorillonite surface, the distinguishing feature is that the results for the TIP4P-Ice model have a more distinct structure at the clay mineral surface compared to the other water models. For the kaolinite siloxane surface, there is almost no difference in structuring between water models in the atomic density profiles. Here the charge of the montmorillonite and the counter balancing sodium cations could be inducing a greater structural difference between the water models as compared to the uncharged kaolinite siloxane surface.
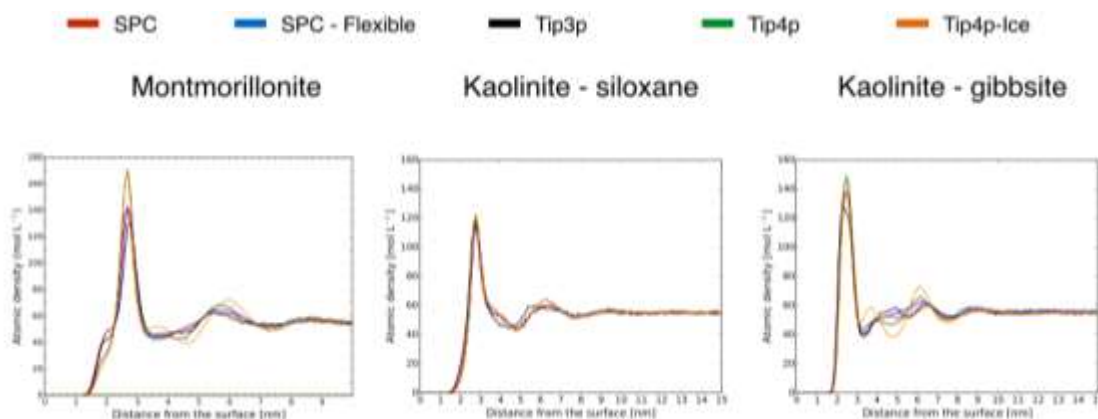
Figure 2-5. Atomic density profiles for montmorillonite (left), kaolinite siloxane surface (center), and kaolinite gibbsite surface (right) showing results for the oxygen atom of each of the water models.

For the hydroxylated gibbsite surface of kaolinite there is again a much more distinct water structure for results using the TIP4P-Ice model. We can also see that the SPC and SPC-Flexible models have much more diffuse second layers (Figure 2-6). The transition to distinct second layers is observed with the TIP3P water model. Results for the TIP4P model looks are similar to those derived for the TIP4P-Ice system.
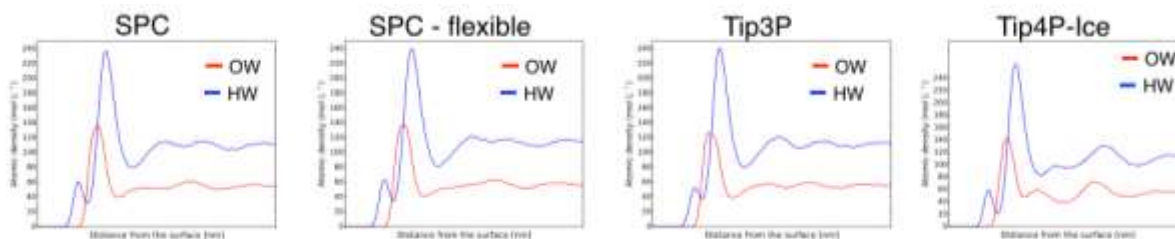
Figure 2-6. Atomic density profiles for the water oxygen (red) and water hydrogen (blue) at the kaolinite gibbsite (hydrophyllic) surface.

2.4.1.2. Water orientation

The orientation of the water molecules with respect the basal surface of the clay mineral is investigated by computing two angles: θ and ϕ (Figure 2-7). The θ angle describes the rise of the water oxygen from the clay surface and is defined as the angle created between the xy plane in the surface and the vector connecting the hydrogen atoms. The ϕ angle describes the rotation of the water molecule on the clay surface and is defined with a zero value when the vector connecting the hydrogen atoms aligns with the x-axis. For the simulations presented here, the x-axis is aligned with the a-axis. For each of the angle calculations, bins are selected to ensure an equal surface area is sampled per bin in spherical space.
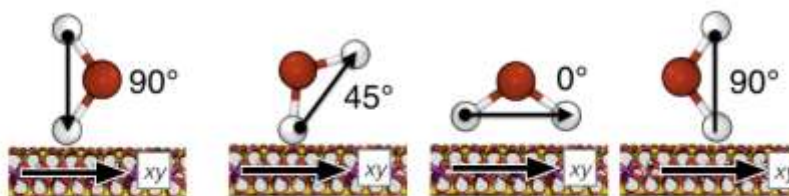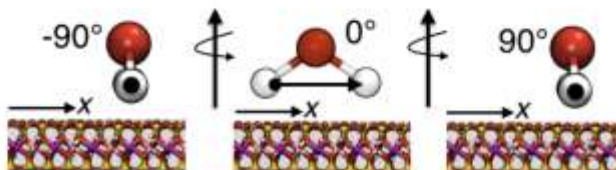
Figure 2-7. Measurement scheme for describing water orientation with respect to clay mineral surface. θ angle describes the rise of the water oxygen from the clay surface and is defined as the angle created between the *xy* plane in the surface and the vector connecting the hydrogen atoms (top). ϕ angle describes the rotation of the water molecule on the clay surface and is defined with a zero value when the vector connecting the hydrogen atoms aligns with the *x*-axis (bottom). For the simulations presented here, the *x*-axis is aligned with the *a*-axis.
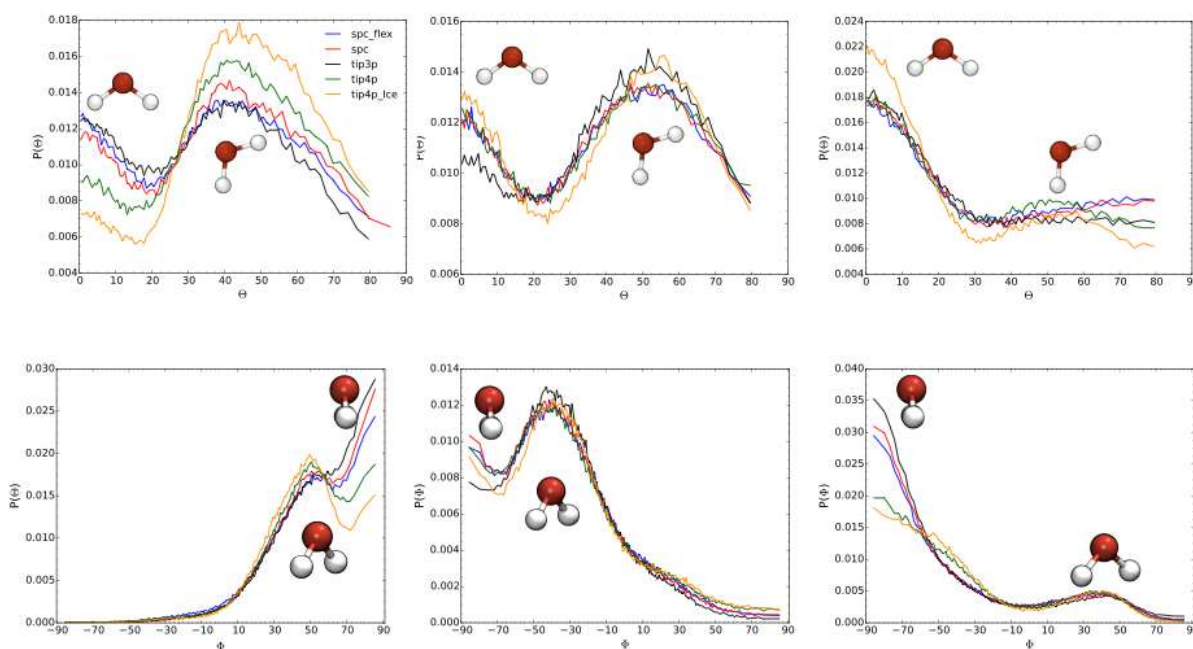
Figure 2-8. Orientation of water molecules on the montmorillonite surface (left), kaolinite siloxane surface (center), and kaolinite gibbsite surface (left) as a function of water model. Top graphs represent the average rise of the water molecules and bottom graphs represent the average rotation of water molecules on the surface of the clays. Only water molecules contained within the first water layer are considered.

Figure 2-8 illustrates the orientational distribution for the five water models over each clay mineral surfaces. Only water molecules contained within the first water layer are considered. In general, there is no difference between the orientational distributions associated with each water model over the same surface. The differences occur when comparing among clay mineral surfaces.

For montmorillonite, the majority of the water molecules take on two configurations with respect to rise from the surface; first, a configuration where the vector connecting the hydrogen atoms is parallel to the surface plane and, second, where the water molecule is elevated by about 40-45°. Water molecules associated with SPC, SPC-Flex, and TIP3P all have similar probabilities of being found in these configurations. However, the probability of finding the TIP4P water molecules in the first configuration is lower as compared to finding this water molecule in the second configuration. This phenomenon is even more pronounced for the TIP4P-Ice model. This behavior is also consistent with what is observed with the kaolinite siloxane surfaces. On the gibbsite surfaces of kaolinite the most likely configuration occurs when the vector connecting the hydrogen atoms is parallel to the xy plane, though there are still some water molecules that adopt the 45° configuration.

It should be noted that these results are for dynamic systems and there should be a non-zero probability for every configuration. Additionally, the graphs appear truncated because the last bin encompasses about 75° to 90° to ensure an equal surface area is sampled per bin in spherical space. In looking at the rotational distributions of water molecules above the clay surfaces, it is the shape of the graph that is important but not the absolute value of ϕ. This is because we are not matching the crystallographic planes of clay but only the x-axis. Therefore, what is important here are the number of peaks and the magnitude of ϕ at which the peaks occur.

Water molecules are found in two rotational configurations on the basal surface of montmorillonite. The first is a rotation of 50° between the normal to the surface and the vector connecting the hydrogen atoms. Here all the water models have roughly the same probability of being in this configuration. The second is a rotation of 90° between the normal to the surface and the vector connecting the hydrogen atoms. For this case there is a slight difference between the water models with the three-site models preferring this configuration to the four-site models. For the kaolinite siloxane surface, again there are two configurations that are preferred -50° and -90° configurations. For the kaolinite gibbsite surface, there are again two configurations that are favored one at -90° and one at 40°. The water models all have the same probability at 40° but the three-site models have more distinct peak at -90°.

Two-dimensional distributions of water oxygen in the xy plane are shown in Figure 2-9. Only waters found in the first water layer are included in these profiles. Cutoff criteria are chosen as the minimum between the first two oxygen peaks in the one-dimensional oxygen profiles shown in Figure 2-5. The cutoff distance varies between clay mineral-water systems. Darker regions correspond to a higher oxygen density. Clay surface atoms are overlaid onto the oxygen profiles for reference. Oxygen distributions are averaged over the clay mineral surface and the results for average values over the surface of one clay mineral unit cell are presented.

The density distributions indicate a clear preference for water oxygen atoms to be located in the center of surface ring structures. Waters above the kaolinite siloxane rings have a more diffuse density profile as compared to the kaolinite gibbsite and montmorillonite density profiles. Distributions of the water oxygens for each water model in the *xz* and *yz* planes are presented in Figure 2-10 and Figure 2-11, respectively. Results for these perspectives indicate the distinct first layer of adsorbed water and the increasingly diffuse nature of the subsequent water layers. Lateral structure observed in the first water layer is related to the type of interactions of water with a charged clay layer (montmorillonite), with formation of hydrogen bonds (kaolinite gibbsite), or with minimal interaction (hydrophobic with kaolinite siloxane).
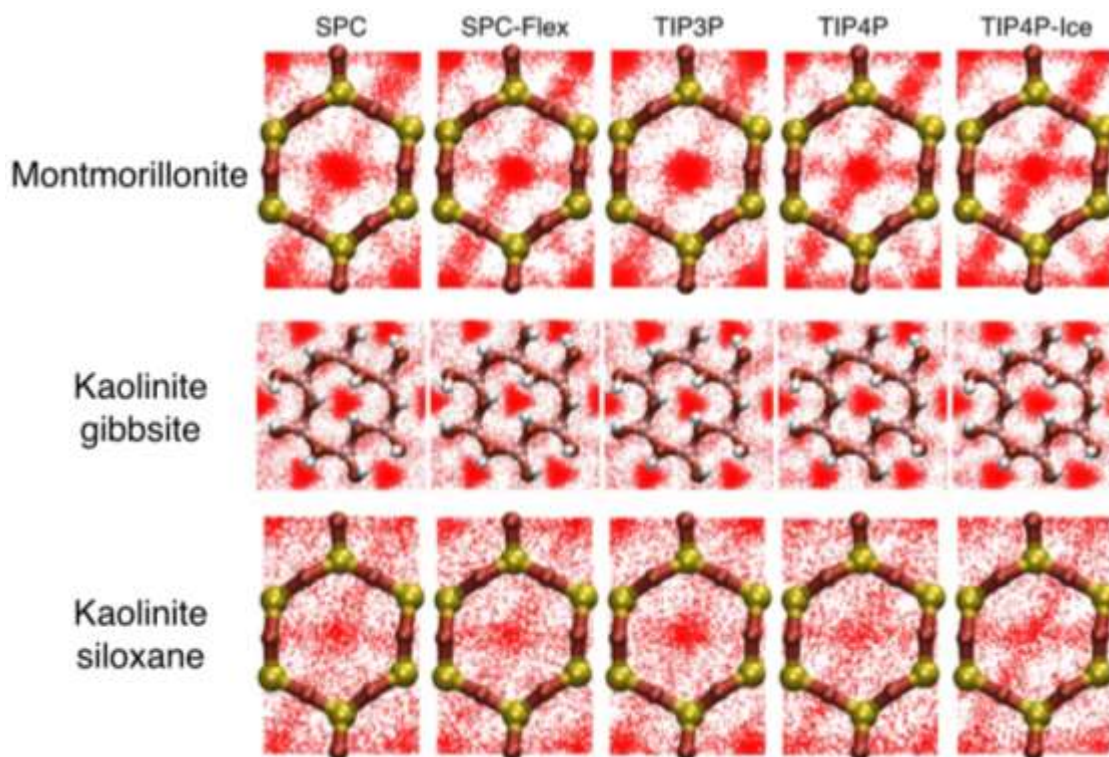
Figure 2-9. Two-dimensional distributions of water oxygen atoms (red) on the surface of the clay minerals are shown in the *xy* plane. Characteristic structure of basal surface of clay is overlaid for reference. Atoms are colored yellow for silicon, red for oxygen, white for hydrogen, and pink for aluminum. Only waters in the first water layer overlaid in the distributions.
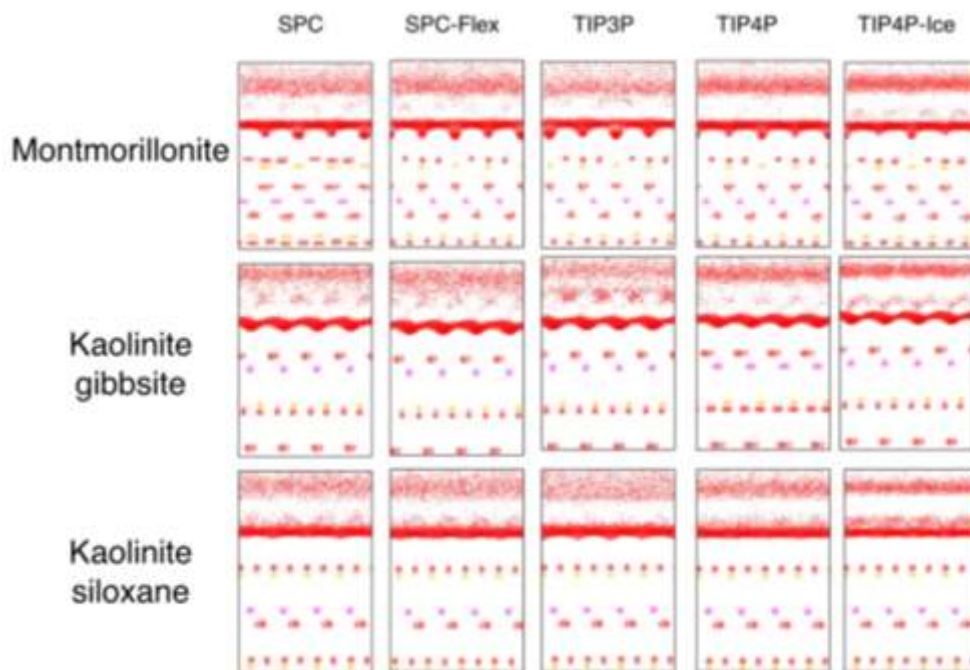
Figure 2-10. Two-dimensional distributions of water oxygen atoms (red) on the surface of the clay minerals are shown in the *xz* plane. Atoms associated with the clay minerals are colored yellow for silicon, red for oxygen, pink for aluminum, and purple for magnesium. Only waters in the first and second layers are included in the water distributions.
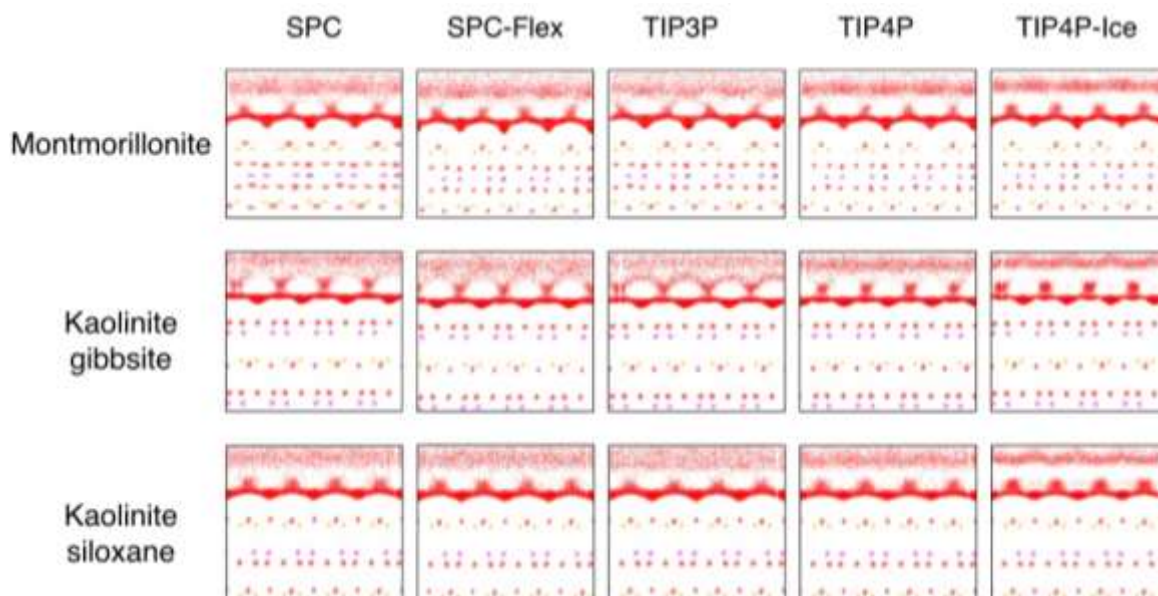
Figure 2-11. Two-dimensional distributions of water oxygen atoms (red) over the surface of the clay minerals are shown in the *yz* plane. Atoms associated with the clay minerals are colored yellow for silicon, red for oxygen, pink for aluminum, and purple for magnesium. Only waters in the first and second layers are included in the water distributions.

20

2.4.2. Dynamic properties

Water diffusion coefficients in the *xy* plane were examined as a function of distance from the surface for each of the water models. Individual diffusion coefficients were calculated for four regions based on minimum between peaks in the one-dimensional atomic density profiles. To calculate the diffusion coefficients, first the *X* and *Y* mean square displacements (MSD) in the *xy* plane were calculated as a function of distance from the surface. The maximum MSD value as a function of the window size was then used to select the reported diffusion coefficient. While bulk MSD values are monotonically increasing functions, planar MSD functions are not. This is because they are weighted by the number of molecules still within the layer at time *t*. There is no reentry to a layer once a molecule has left. Diffusion coefficients (in units of m^2/s) were calculated from three independent simulations and averaged (Figure 2-12).
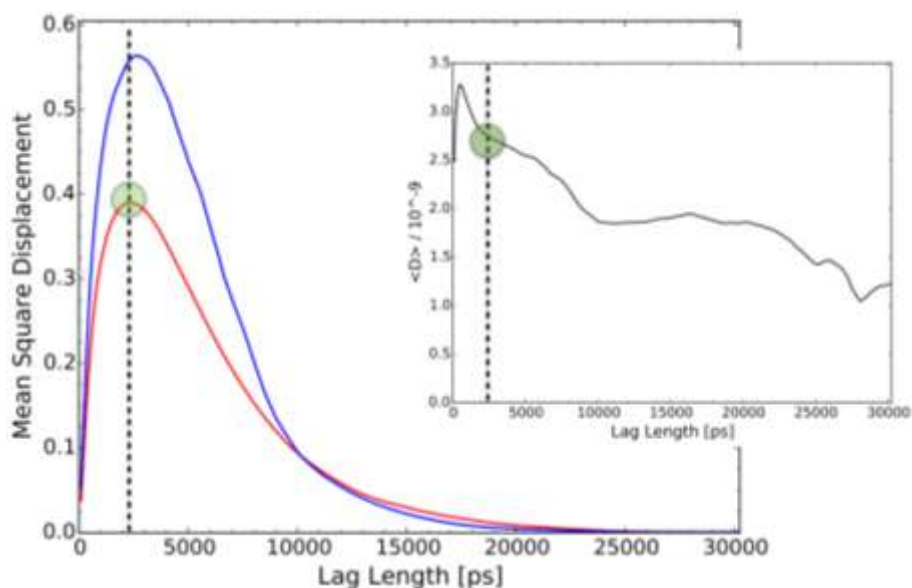
Figure 2-12. Diffusion coefficients are calculated from the point of maximum value in the *x* and *y* mean square displacements as a function of lag length.

In general, values for water diffusion coefficients are smallest closest to the mineral surface and increase further away from the surface reaching a maximum in the bulk (Figure 2-13). Overall, TIP4P-Ice models exhibit the slowest diffusing water molecules followed by SPC, SPC-Flexible, and TIP4P which all have similar diffusion coefficients. TIP3P simulations have generally the fastest diffusion values for water independent of the type of clay mineral or distance from the surface. Diffusion coefficients derived for the kaolinite gibbsite surface are relatively flat and do not appear to depend on water layer.
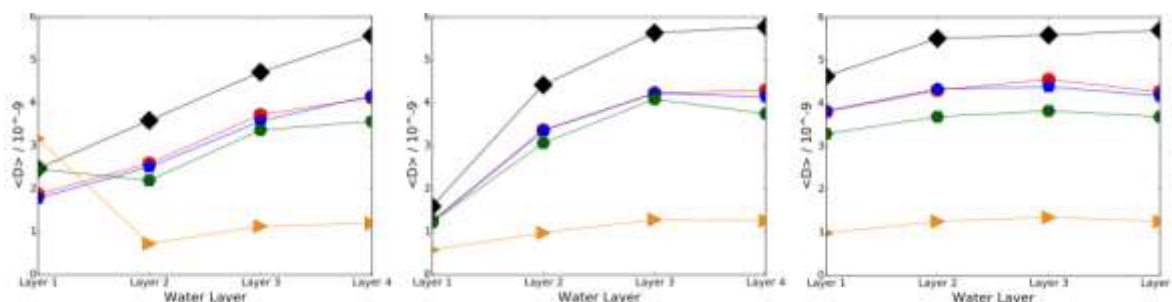
Figure 2-13. Diffusion coefficients for water on montmorillonite surface (left), siloxane kaolinite surface (center), and the gibbsite kaolinite surface (right) for SPC (red), SPC-Flexible (blue), TIP3P (black), TIP4P (green), and TIP4P-Ice (orange). Error bars are smaller than symbols.

2.5. References

Berendsen, H.J.C., van der Spoel, D., and van Drunen, R. (1995) GROMACS: A message-passing parallel molecular dynamics implementation. *Computer Physics Communications*, 91(1-3), 43-56.

Bish, D.L. (1993) Rietveld refinement of the kaolinite structure at 1.5 K. *Clays and Clay Minerals*, 41, 738-744.

Cygan, R.T., Liang, J.-J., and Kalinichev, A.G. (2004) Molecular models of hydroxide, oxyhydroxide, and clay phases and the development of a general force field. *Journal of Physical Chemistry B*, 108(4), 1255-1266.

Jorgensen, W.L., Chandrasekhar, J., Madura, J.D., Impey, R.W., and Klein, M.L. (1983) Comparison of simple potential functions for simulating liquid water. *Journal of Chemical Physics*, 79(2), 926-935.

Teleman, O., Jonsson, B., and Engstrom, S. (1987) A molecular dynamics simulation of a water model with intramolecular degrees of freedom. *Molecular Physics*, 60(1), 193-203.

Vega, C., Sanz, E., and Abascal, J.L.F. (2005) The melting temperature of the most common models of water. *Journal of Chemical Physics*, 122(11), 114507.

3. METHANE HYDRATE NUCLEATION AT CLAY MINERAL SURFACES

3.1. Molecular Models

We use molecular dynamics (MD) to examine three clay mineral surfaces—pyrophyllite, montmorillonite, and kaolinite—to investigate the nucleation and growth of methane cage (clathrate) structures, as precursors to the formation of methane hydrate. Pyrophyllite is a phyllosilicate mineral with a layered structure composed of tetrahedral (T) silicate layers and octahedral (O) alumina layers joined through the sharing of oxygen atoms to form a TOT structure. The monoclinic unit cell formula for pyrophyllite is $Al_2Si_4O_{10}(OH)_2$ with dimensions 0.51600 nm x 0.89660 nm x 0.91920 nm in the a, b, and c crystallographic directions, respectively. Montmorillonite is a smectite clay mineral with a similar layered structure as pyrophyllite. However, in montmorillonite magnesium (Mg^{2+}) is substituted for octahedral aluminum (Al^{3+}) creating a negative charge that is compensated by interlayer sodium cations. The monoclinic unit cell formula is $NaSi_8Al_3MgO_{20}(OH)_4$ with dimensions 0.51600 nm x 0.89660 nm x 0.9347 nm in the a, b, and c crystallographic directions, respectively. Kaolinite is a layered aluminosilicate mineral composed of a tetrahedral silicate bonded to an octahedral alumina layer through shared oxygen atoms. This layering forms a TO structure with two distinct surfaces that form on the (001) basal cleavage plane: an aluminum hydroxide surface and a siloxane surface. There are no atomic substitutions in the kaolinite model and therefore no charge balancing counter ions are required in the structure. The triclinic crystal structure for kaolinite is based on the neutron diffraction study of Bish et. al. (1993) and has unit cell parameters $a = 0.51535$ nm, $b = 0.89419$ nm, $c = 0.73906$ nm, $\alpha = 91.926°$, $\beta = 105.046°$, $\gamma = 89.797°$.

Initial configurations of each molecular model were built over several stages (Figure 3-1). First, each of the three clay systems were expanded to 24 x 14 x 2 in the a, b, and c directions, respectively. Next 600 methane hydrate SI unit cells were melted at $T = 425$ K and $P = 100$ bar for 2 ns to unsure no residual structure remained. Water and methane were then incorporated into the pore space of the clay mineral before being equilibrated using MD simulations for at least 25 ns at $T = 300$K and $P = 1$ bar in the *NPT* ensemble. Separate trials were initiated with different velocity profiles and were run for varying simulation times to ensure independent starting configurations. Finally each system was allowed to evolve at the chosen temperature and pressure being studied.
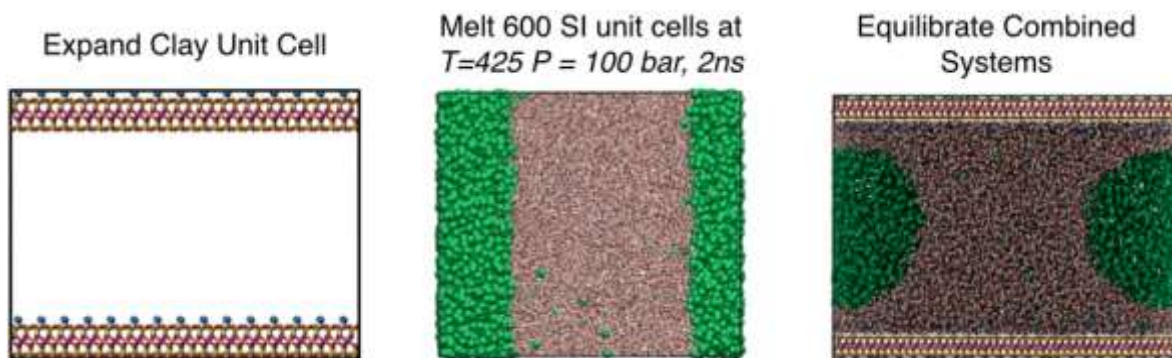
Figure 3-1. Initial configurations of methane-water-clay system built over several MD simulation steps, including expanding the clay unit cell (left), randomizing water and methane (center), and combining the two systems to form a nanopore and equilibrating (right).

We first examined the initial methane distributions for the montmorillonite and kaolinite nanopore systems. Both montmorillonite surfaces are identical while the two kaolinite surfaces are characterized by significantly different surfaces. One surface of kaolinite is hydrophilic and is similar to the hydroxylated gibbsite ($Al(OH)_3$), while the other surface is characterized by a relatively hydrophobic siloxane surface comprised of ditrigonal siloxane rings. For montmorillonite, the methane bubble is roughly centered in the simulation cell, and the methane does not significantly interact with the clay mineral surface (Figure 3-2 and Figure 3-3). The layer of counterbalancing sodium ions is clearly observed in both images above the bottom and below the top surfaces. In contrast, the methane bubble in the kaolinite pore is located much closer to the hydrophobic siloxane surface which also includes a thick layer of methane coverage. Methane molecules do not interact with the hydrophilic gibbsite surface of kaolinite (Figure 3-3).
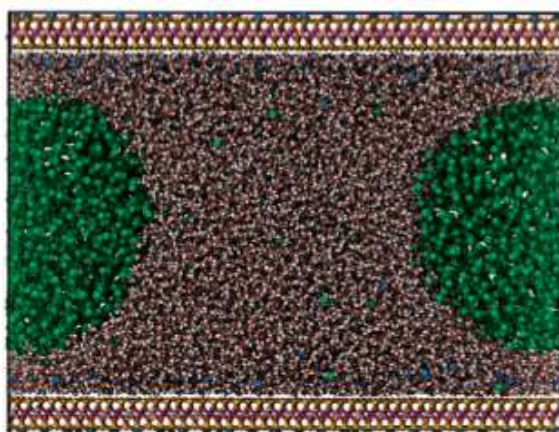
Figure 3.2. MD snapshot of the initial conditions for a montmorillonite nanopore. In the nanopore formed by the expanded montmorillonite interlayer, the methane (green) forms a bubble surrounded by water molecules (red and white). The counterbalancing sodium ions are shown in blue and can be seen near the montmorillonite surface.
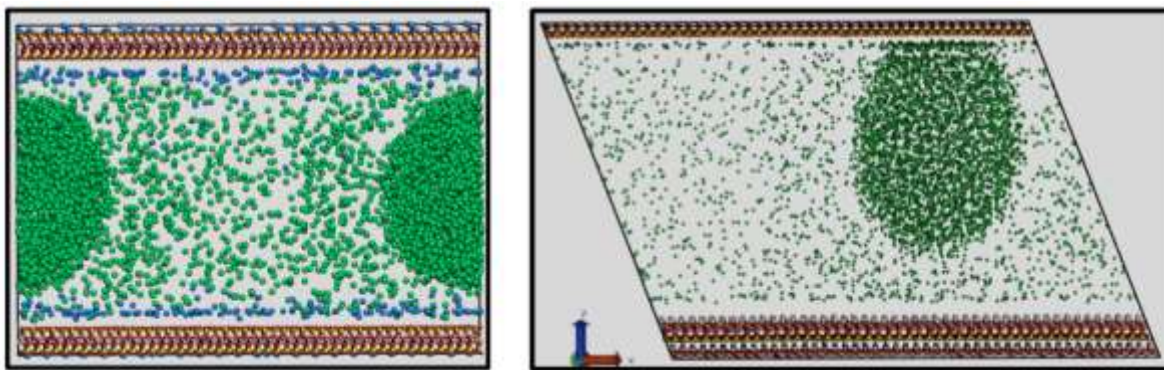
Figure 3-3. MD snapshot of the initial disposition of the methane bubble in montmorillonite (left) and kaolinite (right) nanopore systems. The top and bottom montmorillonite surfaces are identical, while the two kaolinite surfaces have different character: hydrophilic on top surface and hydrophobic on bottom. Water molecules have been removed for clarity. Methane atoms are indicated by green spheres; other atoms are colored are colored blue for sodium, white for hydrogen, red for oxygen, yellow for silicon, pink for aluminum, and purple for magnesium.

3.2. Methods

Molecular dynamics simulations were performed using the GROMACS simulation package (Berendsen et al., 1995). GROMACS is an open source software program for massively parallel MD simulations. A leap-frog integrator was used to integrate Newton's equations of motion. A time step of 2 fs was used for all production runs. The pressure was controlled using an anisotropic Parrinello-Rahman barostat with a time constant of 4 ps and a compressibility of 4.5 x 10^{-5}. In both equilibration and production runs, temperature was controlled using the Nose-Hoover thermostat with a time constant of 2 ps. Full periodic boundary conditions were applied. A cutoff of 10 nm was used for short-range interactions. Long-range electrostatic interactions were modeled with a particle-mesh Ewald method using a Fourier grid spacing of 0.12 nm. Lorentz-Berthelot mixing rules were employed. The SETTLE algorithm is used to model rigid water models, and the normally flexible clay hydroxyl bond lengths are held rigid as well. Simulations were run for a microsecond and positions and velocities are sampled every 0.5 ns while energies are sampled every 10ps.

The clay mineral systems are modeled using the Clayff force field (Cygan et al., 2004) and the water was modeled using the TIP4P-Ice force field. Methane parameters are based on the work of Goodbody et al. (1991) but were re-parameterized to better match the experimental methane solubility values in water from Rettich et al. (1981).

3.3. Results and Discussion

3.3.1. Methane distribution and cage development

Molecular dynamics simulations where run at hydrate-forming conditions within the thermodynamic phase boundary for methane hydrates (Figure 3-4). The number of trials and

specific conditions for each trial are summarized in Table 3-1. Though each of the conditions is within the thermodynamic phase boundary for methane hydrates, no clathrate cages, representative of methane hydrates, were formed during the simulation time for $T = 260$ K and $P = 500$ bar.
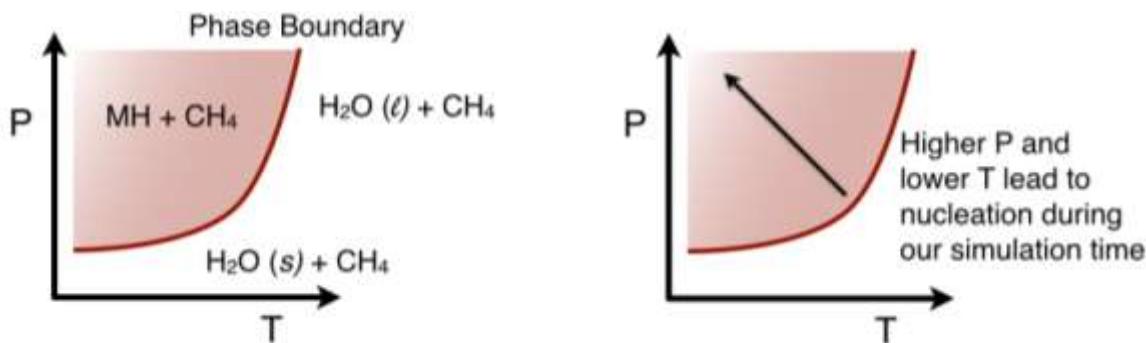
Figure 3-4. MD simulations were run at hydrate-forming conditions within the thermodynamic phase boundary for methane hydrates as indicated in the schematic phase diagrams above.

Table 3-1. Clay minerals, conditions, trials, and nucleation events for MD simulations

Clay Mineral	T, P (K, bar)	# Simulations	# Nucleation events
Kaolinite	245, 1000	5	5
Kaolinite	245, 500	5	5
Kaolinite	260, 1000	5	5
Kaolinite	260, 500	5	0
Montmorillonite	245, 1000	5	5
Montmorillonite	245, 500	5	5
Montmorillonite	260, 1000	5	5
Montmorillonite	260, 500	5	0
Pyrophyllite	245, 1000	8	4
Pyrophyllite	260, 1000	8	0

Simulations are monitored for hydrate formation through visual monitoring, tracking methane density distributions, the calculation of the F_4 order parameter, monitoring the potential energy, and calculation cage formation. The methane concentration changes throughout the simulation cell as a system evolves to form hydrate cages. Figure 3-5 and Figure 3-6 illustrate these changes in terms of the methane concentration and bubble distribution. At the beginning of the simulation the majority of the methane resides in a single bubble at the edges of the simulation cell. Hydrate cage formation draws methane molecules out of the methane bubble and dissolves

in water of the pore volume. Figure 3-7 presents the time evolution of methane hydrate cages. Cage formation begins at 100 ns and the rate of formation increases at approximately 200 ns. Figure 3-8 visually presents the corresponding evolution of the most common hydrate cages (5^{12} and $5^{12}6^2$) in the system. Cages begin to form at the methane bubble interface where the methane concentration and the driver towards nucleation, is highest. The cages grow towards the center of the nanopore as the simulation progresses.
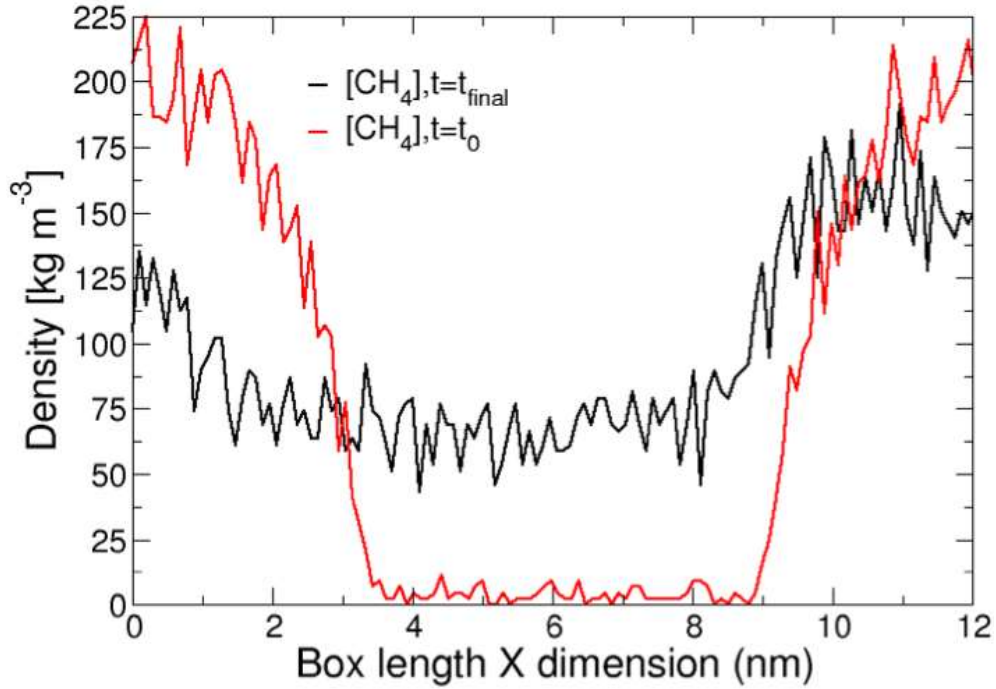
Figure 3-5. Methane concentration as a function of position in *x* direction for montmorillonite nanopore at $T = 245$ K and $P = 1000$ bar. The methane density is averaged over the *yz* plane. The change in the methane distribution can be seen from the beginning (red) to the end (back) of the MD simulation.
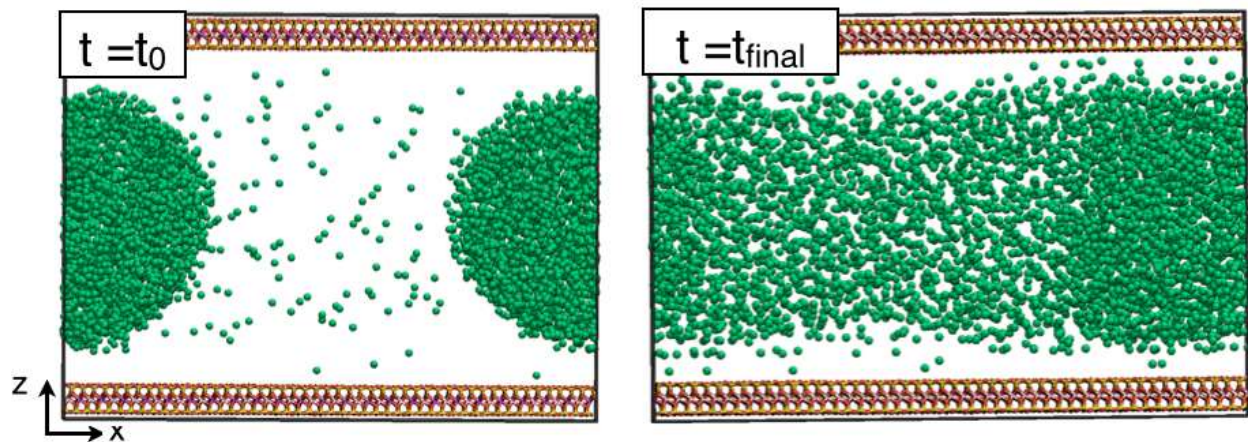
Figure 3-6. Methane distribution in a montmorillonite nanopore at the beginning and end of a microsecond MD simulation at T = 245 K and P = 500 bar. Water molecules have been removed for clarity. Methane atoms are collectively represented by green spheres; blue for sodium ions, white for hydrogen atoms, yellow for silicon atoms, pink for aluminum atoms, red for oxygen atoms, and purple for magnesium atoms.
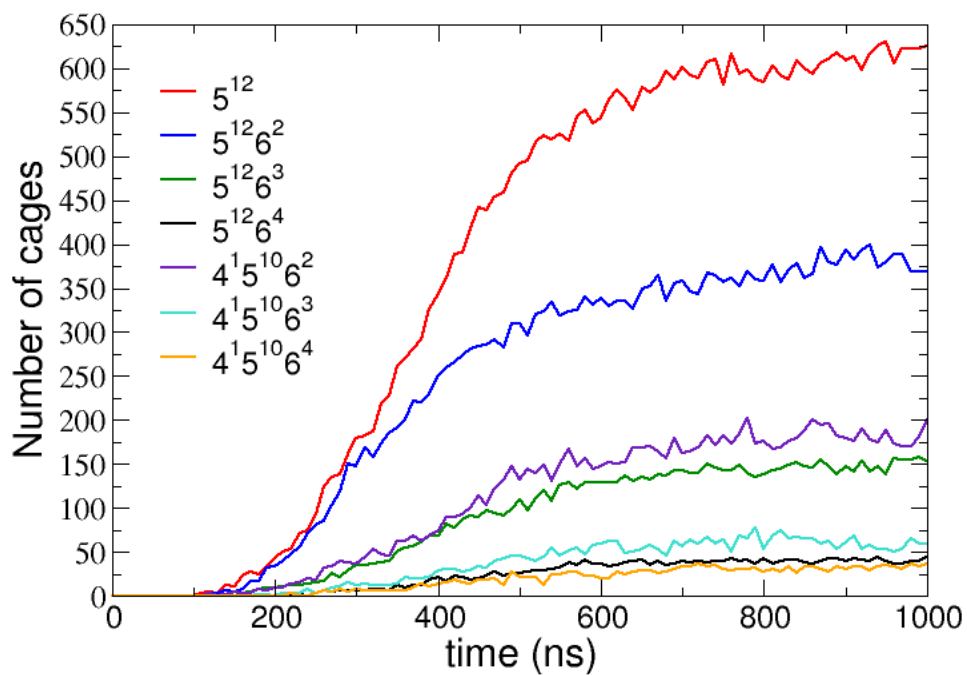
Figure 3-7. Evolution of cage formation from MD simulation of montmorillonite nanopore at T = 245 K and P = 1000 bar.
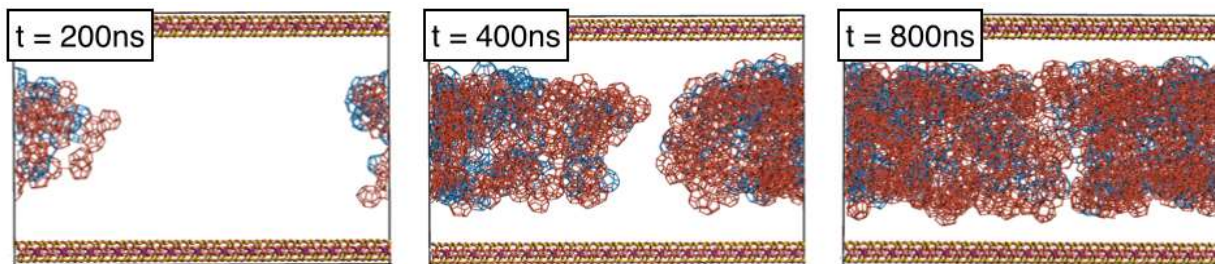
Figure 3-8. Evolution of methane hydrate cages in montmorillonite nanopore. 5^{12} cages (blue) $5^{12}6^2$ cages (red) are are the two most common cages that occur during MD simulation for $T = 245$ K and $P = 1000$ bar. The image is shown in the xz plane.

Figure 3-9 shows the hydrogen-bonding network for the kaolinite nanopore system at the end of a microsecond simulation. Methane molecules have been removed for clarity. Hydrate cages can be seen in the lower right-hand corner of the simulation cell. Figure 3-10 presents the occurrence of 5^{12} cages during the evolution of the simulation as a function of distance from both the hydrophilic and hydrophobic surfaces. The water rings of the 5^{12} cage occur with a higher frequency closer to the hydrophilic gibbsite surface of kaolinite earlier in the simulation than they do at the hydrophobic siloxane surface. To investigate the how surface atoms participate in ring formation, we monitor the number of surface atoms participating in cage formation throughout the simulation. We observe that only half pentagonal rings (5^{12}) and half hexagonal rings ($5^{12}6^2$) contain surface atoms from the clay mineral. Figure 3-11 provides the average number of surface atoms that participate in ring formation during the simulation for each of the five trials run at $T = 245$ K and $P = 1000$ bar. On average there are more atoms on the hydrophilic surface participating in ring structuring than on the hydrophobic surface.

Figure 3-9. A final snapshot taken from a kaolinite nanopore MD simulation at $T = 245$ K and $P = 1000$ bar. Hydrogen bonding of water molecules is indicated (red) in the montmorillonite nanopore. Hydrate cages can be seen in the lower right corner of the nanopore. Methane molecules have been removed for clarity.

29

hydrophilic surface   hydrophobic surface
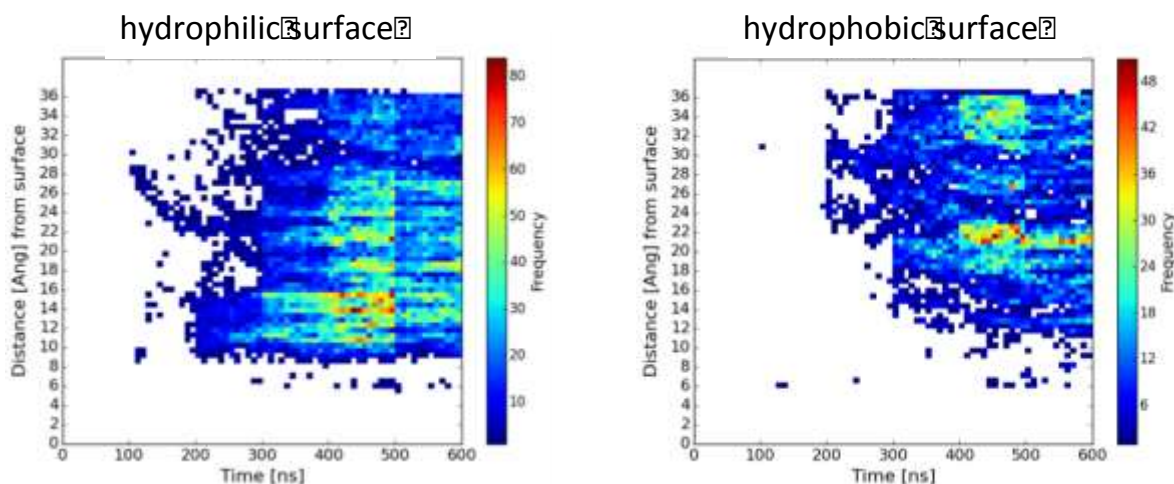
Figure 3-10. Frequency distributions of the occurrence of 5^{12} hydrate cages as the MD simulation of the kaolinite nanopore evolves. Results for both the hydrophilic (left) and hydrophobic (right) kaolinite surfaces are presented. The zero point of the *y*-axis represents the surface oxygen atoms of the kaolinite.

Average number of surface atoms participating in clathrate cages
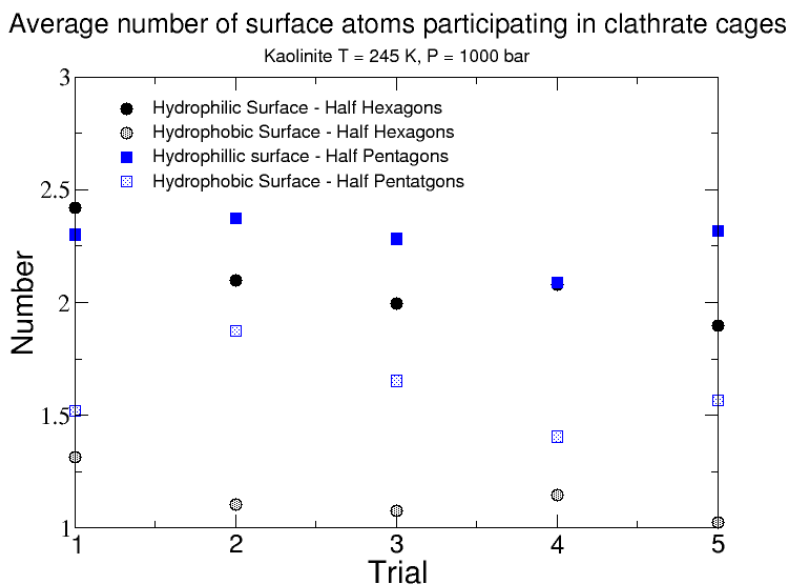
Figure 3-11. Averages of the instantaneous number of surface atoms participating in rings of half pentagonal (5^{12}) or half hexagonal ($5^{12}6^2$) hydrate cages for siloxane and gibbsite surfaces of kaolinite from MD simulation.

3.3.2. Order parameter

Order parameters are quantitative measures of the degree of structurally order in a system. The F_4 order parameter of Hawtin et al. (2008) was developed to distinguish among the different tetrahedral networks that characterize water structures. This four-body order parameter is based on the H-O$\cdots$O-H torsion angle Φ created by two neighboring water molecules and is defined by:

$$F_4 = \cos(3\phi) \tag{1}$$

Values of the F_4 order parameter for bulk methane hydrate and liquid water are close to 0.7 and 0.0, respectively.

Figure 3-12 shows the time evolution of the system averaged F_4 order parameter for pyrophyllite nanopores at the two conditions studied: $T = 245$, P $= 1000$ bar and $T = 260$ K, $P = 1000$ bar. For the first set of conditions, seven of the eight completed trials are presented, and ordering has appeared in three of the seven by the end of the microsecond MD simulation. For the second set of conditions, again seven of the eight trials are presented. In these systems there is no water structuring present by the end of the MD simulation; the water remains in the normal liquid state.

Figure 3-13 provides the time evolution of the system averaged F_4 order parameter for montmorillonite systems for conditions studied: $T = 245$ K, $P = 500$ bar; $T = 245$ K, $P = 1000$ bar; $T = 260$ K, $P = 500$ bar; and $T = 260$ K, $P = 1000$ bar. Results are shown for all five trials at each of the four conditions. Cage formation is present in all systems except at $T = 260$, $P = 500$ bar. Hydrate cage formation occurs earliest in the $T = 245$ K, $P = 1000$ bar system followed by the $T = 245$ K, $P = 500$ bar system, and then the system at $T = 260$ K and $P = 500$ bar.

The F_4 order parameter can be further investigated by dividing the nanopore into regions as done for one of the kaolinite systems at $T = 245$ K and $P = 1000$ bar (Figure 3-14). The simulation cell was divided into five regions beginning at the gibbsite surface region and moving along the z-axis to the siloxane surface. Regions are denoted by color with Region 1 (black) at the gibbsite surface, Region 3 (green) in the central part of the pore, and Region 5 (orange) at the siloxane surface.

Regions 1 and 5 represent the water closest to the kaolinite surface with minimal water structuring that occurs towards the end of the MD simulation. As the simulation proceeds, the order parameter indicates the formation of hydrate structure beginning in Region 2, which is closest to the kaolinite gibbsite surface. This stage is followed by an increase in hydrate cage structure in Region 3, and then later in Region 4 indicating a growth pattern beginning closest hydrophilic surface and extending outward into the bulk and toward the hydrophobic surface.
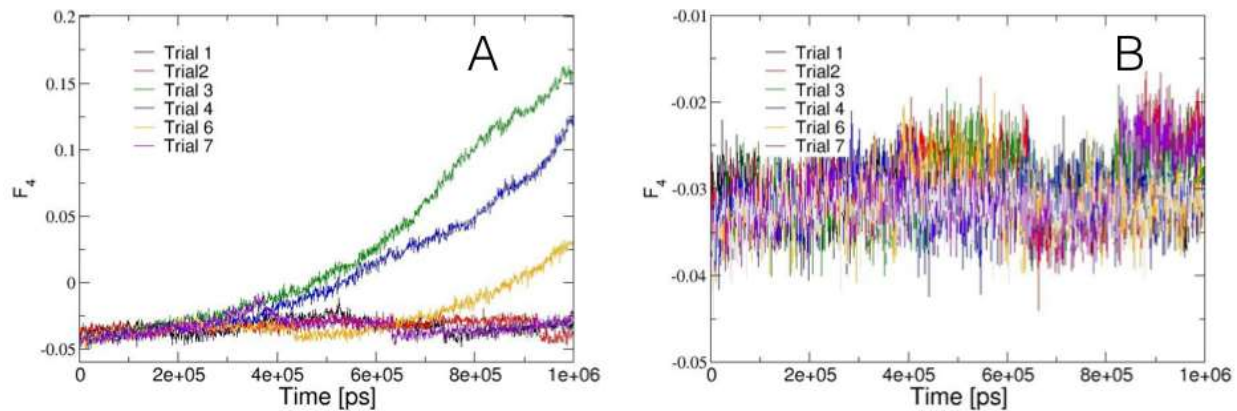
Figure 3-12. Time evolution of the averaged F_4 order parameter for MD simulations of pyrophyllite nanopore at conditions (A) $T = 245$ K, $P = 1000$ bar and (B) $T = 260$ K, $P = 1000$ bar. Results are shown for all trials at each of the two conditions.
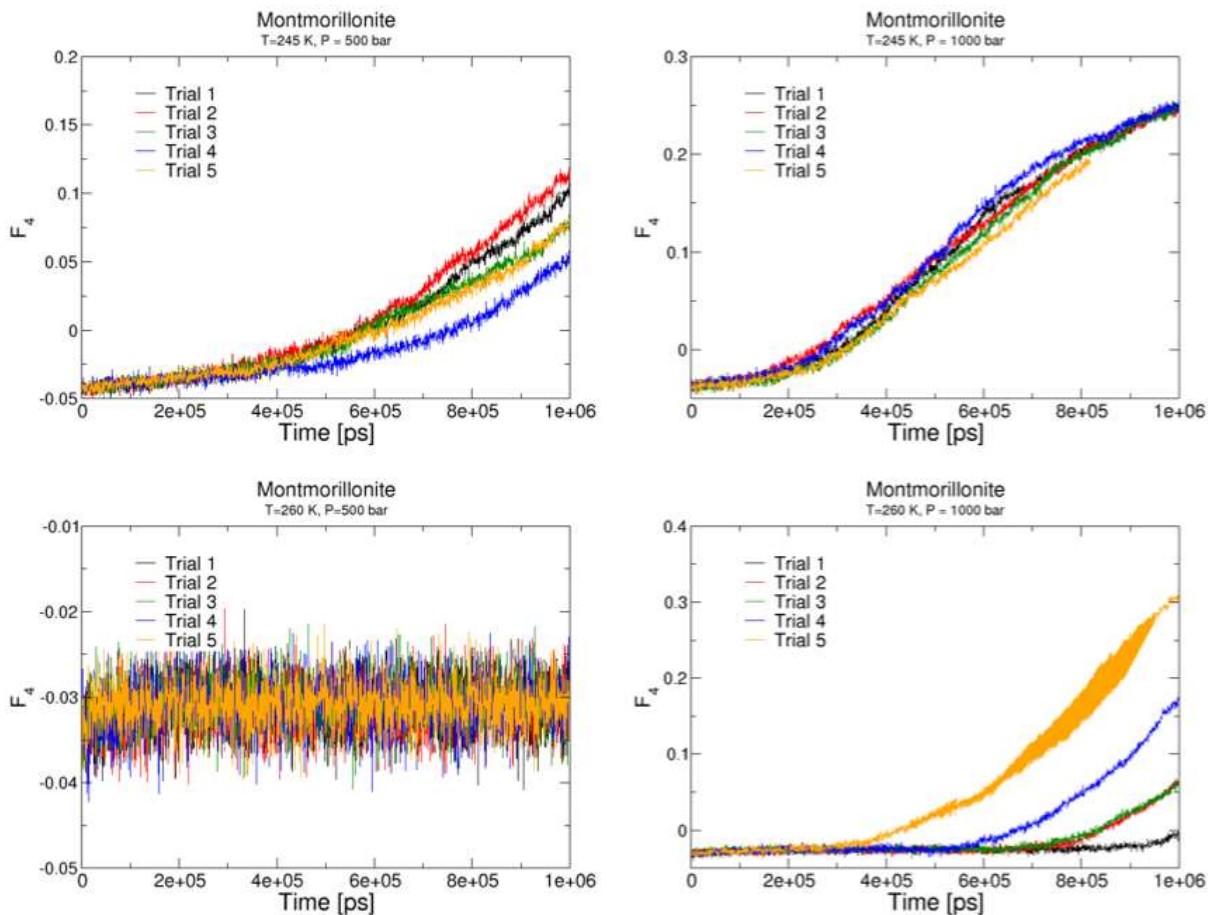
Figure 3-13. Time evolution of the system averaged F_4 order parameter for MD simulations of montmorillonite nanopore at conditions (A) $T = 245$ K, $P = 500$ bar; (B) $T = 245$ K, $P = 1000$ bar; (C) $T = 260$ K, $P = 500$ bar; and (D) $T = 260$ K, $P = 1000$ bar. Results are shown for all five trials at each of the four conditions.
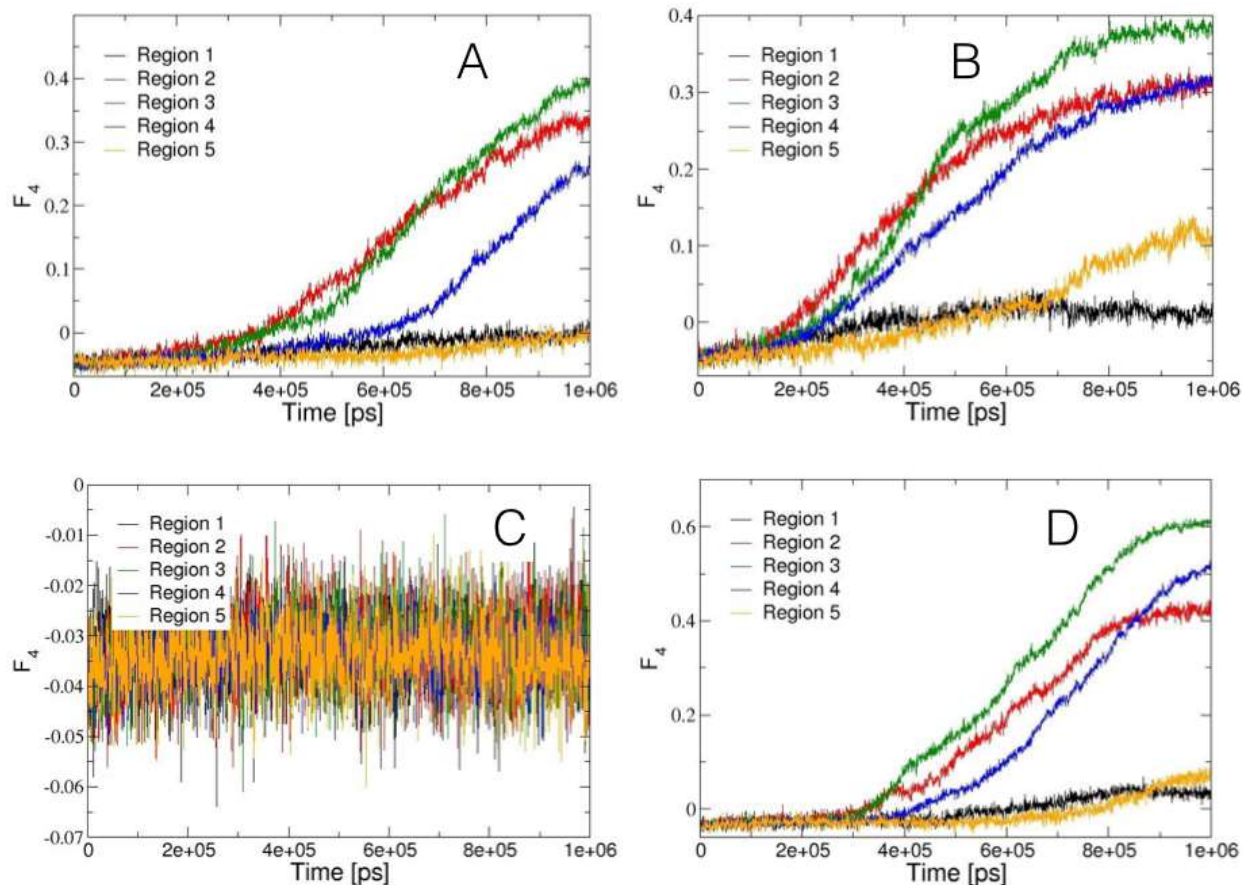
Figure 3-14. Examples of the evolution of the F_4 order parameter for MD simulations of kaolinite nanopore at conditions (A) $T = 245$ K, $P = 500$ bar; (B) $T = 245$ K, $P = 1000$ bar; (C) $T = 260$ K, $P = 500$ bar; and (D) $T = 260$ K, $P = 1000$ bar. Results are shown for different regions in the kaolinite pore: Region 1 (black), Region 2 (red), Region 3 (green), Region 4 (blue), and Region 5 (orange). F_4 values for simulations of liquid water, ice, and methane hydrate are -0.04, -0.4, and 0.7, respectively.

3.4 References

Berendsen, H.J.C., van der Spoel, D., and van Drunen, R. (1995) GROMACS: A message-passing parallel molecular dynamics implementation. *Computer Physics Communications*, 91(1-3), 43-56.

Bish, D.L. (1993) Rietveld refinement of the kaolinite structure at 1.5 K. *Clays and Clay Minerals*, 41, 738-744.

Goodbody, S.J., Watanabe, K., and MacGowan, D. (1991) Molecular simulation of methane and butane in silicalite. *Journal of the Chemical Society Faraday Transactions*, 87(13), 1951-1958.

Hawtin, R.W., Quigley, D. and Rodger, P.M. (2008) Gas hydrate nucleation and cage formation at a water/methane interface. *Physical Chemistry Chemical Physics*, 10, 4853-4864.

Rettich, T.R. Handa, Y.P., Battino, R., and Wilhelm, E. (1981) Solubility of gases in liquids 13. High-precision determination of Henry constants for methane and ethane in liquid water at 275 K to 328 K. *Journal of Physical Chemistry*, 85(22), 3230-3237.

4. SURFACE-ASSISTED FORMATION OF METHANE HYDRATES ON ICE AND NA-MONTMORILLONITE CLAY

4.1. Abstract

Methane hydrates are extremely important naturally-occurring crystalline materials that impact climate change, energy resources, geological hazards, and other major environmental issues. Whereas significant experimental effort has been completed to understanding the bulk thermodynamics of methane hydrate assemblies, little is understood on heterogeneous nucleation and growth of methane hydrates in clay-rich environments. Controlled synthesis experiments were completed at 265-285 K and 6.89 MPa to examine the impact of montmorillonite surfaces in clay-ice mixtures to nucleate and form methane hydrate. The results suggest that the hydrophilic and methane adsorbing properties of Na-montmorillonite reduce the nucleation period of methane hydrate formation in pure ice systems.

4.2. Introduction

Methane hydrates are a class of clathrate compounds that form under high pressure and low temperature conditions (generally greater than 3.5 MPa and less than 280 K) with ice-like cages surrounding one or more methane molecules [1]. Several methane hydrate structures exist, and the two most common types, isometric structure I and structure II, are formed of both small and large H_2O cages. Structure I is built of two small cages consisting of 12 pentagonal faces (5^{12} cages), and six large cages that have 12 pentagonal faces and 2 hexagonal faces ($5^{12}6^2$ cages). The larger unit cell of structure II consists of sixteen 5^{12} and eight $5^{12}6^4$ cages [1].

Methane hydrates form naturally in ocean floor sediments associated with gas vents [1]. Deep-water oil pipelines present ideal thermodynamic (sub-zero temperatures and high pressure) and chemical (methane in contact with sea water) conditions for the formation of methane hydrates that can ultimately lead to pipeline blockages [1]. Large untapped hydrate reserves also exist in the Arctic seafloor and a recent U.S Geological survey estimates that 590 trillion cubic feet (or over 14000 km^3) of methane hydrate is present in the permafrost on the North Slope of Alaska [2-4]. At ambient conditions, methane hydrates decompose to produce methane and water, making them of interest as an energy resource or as potential energy carriers. At the same time, if destabilized through warming or other disruptive processes, natural formations of methane hydrate could release large amounts of methane, a recognized greenhouse gas considerably more impactful to the climate than CO_2 [5] The ability to utilize and control hydrate resources is currently hindered by a lack of fundamental understanding of the impact of geological setting and conditions on the stability and formation of methane hydrates, which are typically found in clay-rich sediments.

Prior work on understanding the formation of hydrates on ice and water [6-17] has revealed several key parameters and stages in methane hydrate growth. The size of the gas-ice contact area correlates directly with the formation of methane hydrate as shown in early work by Barrer and Edge [18]. A study by Wang and coworkers on the kinetics of methane hydrate formation on deuterated ice calculated the activation energy to be 61.5 kJ/mol [19]. Several models have been proposed for methane hydrate formation, including a shrinking ice core model [20,21], a

diffusion model [9], and a quasi-liquid redistribution model [22]. Laboratory investigations have elucidated two recognized stages in hydrate formation on ice [6,7,23]. First, a nucleation event occurs at a high energy surface site or interface such as a crack, step edge, or contact point between ice particles. Hydrate forms, spreading across the ice-grain surface creating a "shell" of hydrate around the ice particles. The second stage of hydrate formation occurs via two potential pathways—hydrate on hydrate growth via diffusion of water through the hydrate shell formed in stage 1, or "sub-shell" hydrate growth from gas diffusion through the hydrate shell to the ice surface. While there is evidence supporting hydrate formation through these stages, additional simulation investigations separating the nucleation events, spreading events, and bulk growth events are required to fully understand their synergy and controlling parameters [24]. Current ongoing work in our laboratories is examining these systems at the molecular scale with simulation to understand growth kinetics in both homogenous and heterogeneous media.

Formation of natural methane hydrates occurs in numerous submarine basins, each exhibiting unique sediment characteristics. Several studies have investigated the stability, kinetics, and spatial distribution of hydrates [25-29] on diverse ocean sediments. Many of these studies, however, focus on methane-saturated water in a stirred reactor and reactions can require several days [11,30,31]. Reactions are limited by mass and heat transfer. In more specialized experimental reactors, Kang and coworkers investigated porous silica and determined that the porous silica surface inhibited the thermodynamics of growth, raising the temperature at which methane hydrate growth commenced by 1-1.5 K [32]. Further studies of hydrate nucleation on porous silica have shown that the smaller the pore size, the greater the growth inhibition effect [33, 34]. The influence of clay mineral surfaces [35] was investigated and found that bentonite particles assist in the formation of methane hydrates, requiring a lower driving force of 0.66 MPa at 4.5 °C (277.65 K) instead of >4 MPa in a stirred liquid reactor. Seo and coworkers investigated methane hydrate formation in the interlayer spaces of Cheto montmorillonite, and found that its higher charge interlayer cation (Ca^{2+} counter cations vs. Na^+ in other montmorillonite samples) negatively affected the promotion of hydrate growth through structuring of the hydrating waters [36].

In this paper, the investigation of Na-montmorillonite clay surface-mediated formation of methane hydrates from a cold, dry, static system of ice and clay is reported. Substrates consisted of pure ice and three relatively low amounts of Na-montmorillonite (5%, 10%, and 15% by weight) mixed with ice. A comparison of the required time for each system to initiate hydrate formation (the nucleation period) is presented and discussed.

4.3. Materials and Methods

Natural Wyoming Na-Montmorillonite (MMT) (SWy-2, Source Clays Repository, administered by the Clay Minerals Society) and UHP grade methane from Trigas were used as received. The surface area of MMT was measured via BET (Micromeritics ASAP 2010) to be 17.55 ± 0.25 m^2/g.

The synthesis procedure is similar to that reported in Stern et al. [8]. Gas-free ice (20.0g) precooled to -26 °C (247.15 K) was pulverized, weighed, and placed in a pre-cooled Teflon cup. For samples containing clay, the ice was pulverized, and then mixed with pre-cooled clay in the

appropriate weight percentage (5, 10, and 15%). The added surface area of the clay varied from 17.55 m^2, to 35.10 m^2, and to 52.65 m^2. These values correspond to an added surface area of 0.84 m^2/g, 1.60 m^2/g, and 2.29 m^2/g of the clay-ice mixtures, respectively. The cup was then capped, and placed in a pre-cooled Parr reactor (Model 4651-High Pressure Vessel, 250 mL volume) located in a programmable chest freezer (Freezer Concepts CH40-13 Chest Freezer). The initial system temperature (freezer and reactor) was -26 °C (247.15 K). After evacuation and purging with pre-cooled N$_2$, and then purging with precooled CH$_4$, the reactor was pressurized to 6.89 MPa with pre-cooled CH$_4$ and allowed to equilibrate. The temperature and internal pressure of the reactor were recorded throughout, as was the temperature of freezer. After approximately 30 minutes, the temperature and pressure stabilized. Undercooling of the reactor to 247 K well below the reaction temperature as found by Stern and coworkers, ensures that the temperature increase of the methane gas during the adiabatic expansion from the precooling chamber into the reaction vessel does not approach the melting point of ice [37].

The freezer was then programmed to warm at 3.5 K/hr. As the temperature increased and exceeded the melting point of water, the reactor achieved an isothermal state as the ice melted. In the presence of free water and ice at 6.89 MPa of CH$_4$, the methane pressure dropped as methane hydrate formed. The time from equilibrium to the inflection of the pressure curve was measured. Specifically, the time from a defined starting temperature of 268.15 K to the divergence of the pressure data curve from the temperature data curve was measured. A control experiment with ice and nitrogen (6.89 MPa) was performed; that data is available in the supporting information.

Data was normalized using the following protocol. A starting temperature for each experiment was set to 268.15 K. The pressure data were then corrected to normalize the pressure for the temperature profile for each experiment and adjust each starting pressure to 6.89 MPa:

$$P_{\text{corrected}} = P_{\text{measured}} - [(P_{\text{start}} - 6.89)T_{\text{measured}}]/T_{\text{start}} \qquad (1)$$

Samples for Raman spectroscopy and powder X-ray diffraction were obtained using the following procedure. Pulverized gas free ice was loaded into a pre-cooled Teflon cup. The cup was capped, and the Parr reactor was sealed. The experiment then proceeded as described above. After 250 minutes, including 100 minutes in the hydrate forming region, the pressurized reactor was cooled to 248.15 K. The reactor was vented, and the capped Teflon sample cup was removed and placed in a container with liquid nitrogen (77.2 K).

To obtain Raman data, the cooled sample was removed from the liquid nitrogen, placed into a quartz cuvette that had been cooled in liquid nitrogen before being placed in the Macro chamber of a Horiba T64000 Raman Spectrometer fitted with 600 grooves/mm gratings. A green laser (514.532nm laser at 10mW before entering the instrument) was used for excitation. The instrument was calibrated by placing a sample of powdered LDPE (in a quartz cuvette holder) into the Macro chamber and acquiring a spectrum. The methane-hydrate spectrum shown was captured using 10 accumulations of 10 seconds. The time from Parr reactor depressurization to complete the data capture was less than 45 minutes.

Powder X-ray diffraction data using a Bruker Venture Single Crystal diffractometer was obtained in the following manner. The synthesized methane hydrate powder was scooped out of the LN_2 cooled beaker and onto either a glass fiber or on Mylar-tipped loops which was subsequently mounted quickly onto the instrument. Both materials add minimal signal to the pattern in terms of sharp reflections in the 2θ diffraction pattern. The fast transfer of the sample was necessary to prevent warming and decomposition of the methane hydrate material. Once mounted, the sample was held under a cold-stream of gaseous N_2 at 100 K. A micro-focused X-ray source (Cu radiation) was employed for XRD analysis with a spot size of ~100 micron for the beam at the sample location. Incident beam mirror optics conditioned the x-ray beam to a monochromatic wavelength. The powder was spun on the phi axis to improve randomization of the powder during collection. A 60-second frame time was employed and data were collected using a CMOS Photon 100 detector. Area detector data were reduced to a 1D pattern via APEX II software and the subsequent patterns were analyzed via JADE (V9.6) software for phase identification.

4.4.   Results

Experimental hydrate nucleation runs, following the above procedure, result in the reproducible formation of methane hydrate with remnant ice in the pressure vessel. The starting conditions of 6.89 MPa and 268K (undercool $\Delta T = 5$K) were chosen to be within the ice and methane hydrate stability region. Owing to the absence of liquid water, however, the formation of methane hydrate under these conditions is kinetically unfavored [37]. These starting conditions, therefore, allow the system to equilibrate for <60 minutes without the risk of hydrate formation.

All experiments proceed following identical steps as presented by Stern and coworkers [8] and Staykova and coworkers [7]. At initial conditions, the reaction vessel is at 6.89 MPa pressure, and ice and methane exist in equilibrium. These phases persist as the reaction vessel temperature increases until reaching the melting point of ice (Figure 4-1). Near 273 K, liquid water appears [7,8] in the system on the surface of the ice grains and the reaction vessel enters an isothermal period. Prior work using SEM [6,7] shows that in a pure system the first methane hydrate crystals form at the interstices of the ice grains once liquid water is present. The exothermic nature [6,12] of the hydrate formation reaction further drives the phase change of H_2O and therefore hydrate formation reaction as well. Growth continues across the surface of the ice grain as the methane hydrate forms from the water present. At the temperature ramp rate used in these experiments, the reaction vessel reaches the methane hydrate dissociation point (~282 K) before the water is completely consumed in the reaction. As the focus of this work is the initial formation of hydrate, complete conversion of the solid water to methane hydrate was unnecessary. Raman spectroscopic data and powder XRD were used to confirm both the presence of sI hydrate and ice after 240 minutes. The Raman peaks present at 2907 and 2914 cm^{-1} are characteristic of the methane stretching modes of CH_4 molecules enclosed in hydrate cages [38] (Figure 4-3). Further confirmation is provided by the collected powder XRD pattern which clearly shows overlapping ice and methane hydrate peaks (Figure 4-3). A relative intensity ratio analysis of the XRD data suggests that the sample is approximately 42 wt% methane hydrate with the balance being composed of ice. Visual inspection of the reaction products in the vessel indicate the characteristic hydrate texture and popping sound associated with hydrate decomposition and methane release.
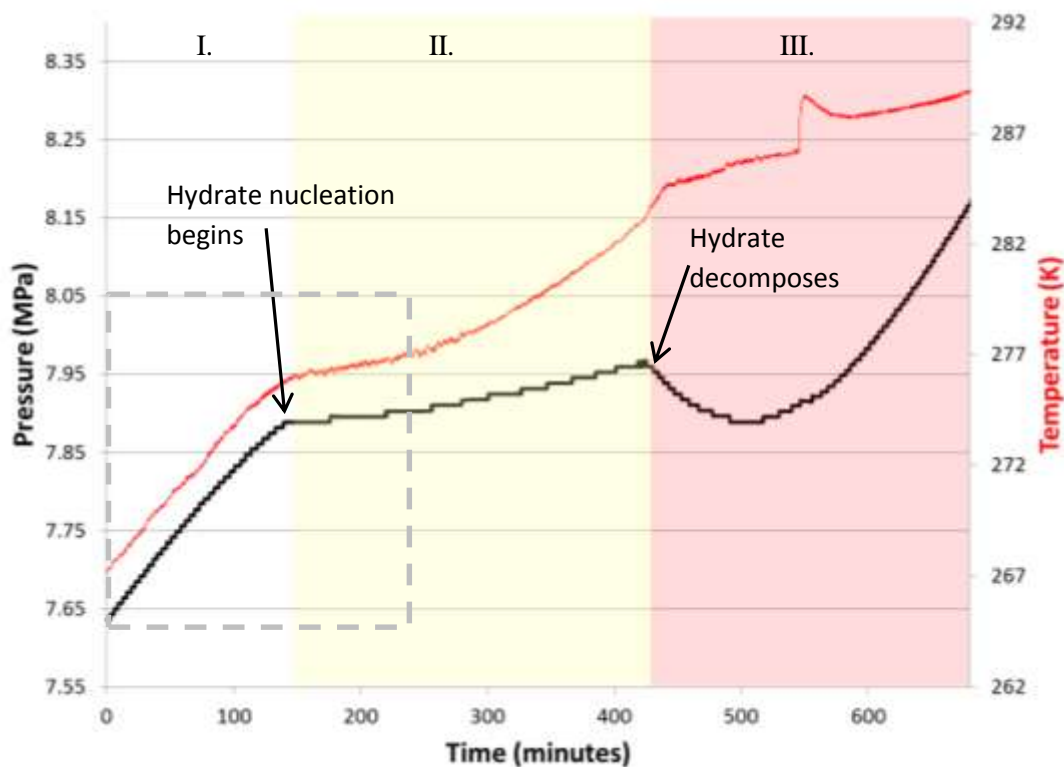
Figure 4-1. Pressure versus time data of methane + ice reaction with phase spaces delineated by shaded areas. Black line denotes the temperature data, and red line denotes the pressure data. Non-shaded area (I) represents the phase space where ice and methane are present. Yellow-shaded area (II) represents the phase space where ice, water, methane, and methane hydrate coexist. Red-shaded area (III) represents the area in which methane hydrate is no longer stable, and decomposes to water and methane. Gray-dashed outline box at left is expanded in Figure 4-2. Full phase diagram for the methane-ice-methane hydrate system is provided by Stern and coworkers [37].
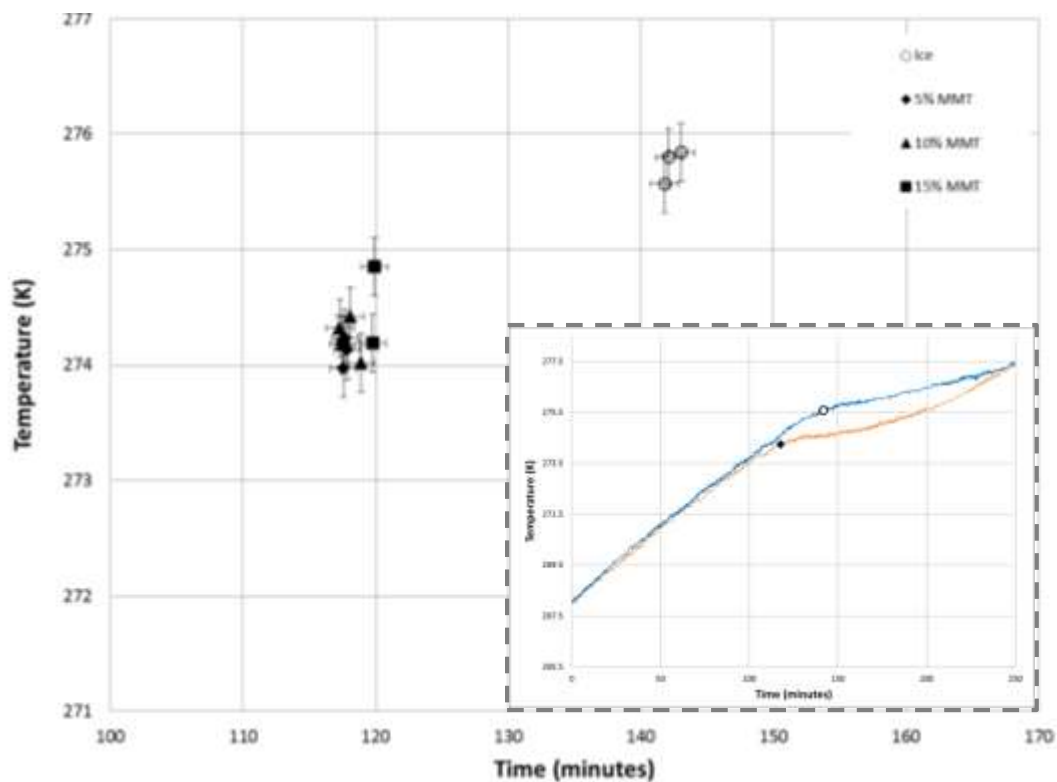
Figure 4-2. Temperature and time coordinates of the pressure deflection point for methane-ice and methane-ice-MMT clay samples. Filled black data points represent the deflection point of clay containing reactions, open data points represent pure ice and methane reactions. For clarity, one temperature data set each of the ice (blue line) and the 5% MMT reactions (orange line) is included in the lower right inset to show the course of the reaction progress over time.
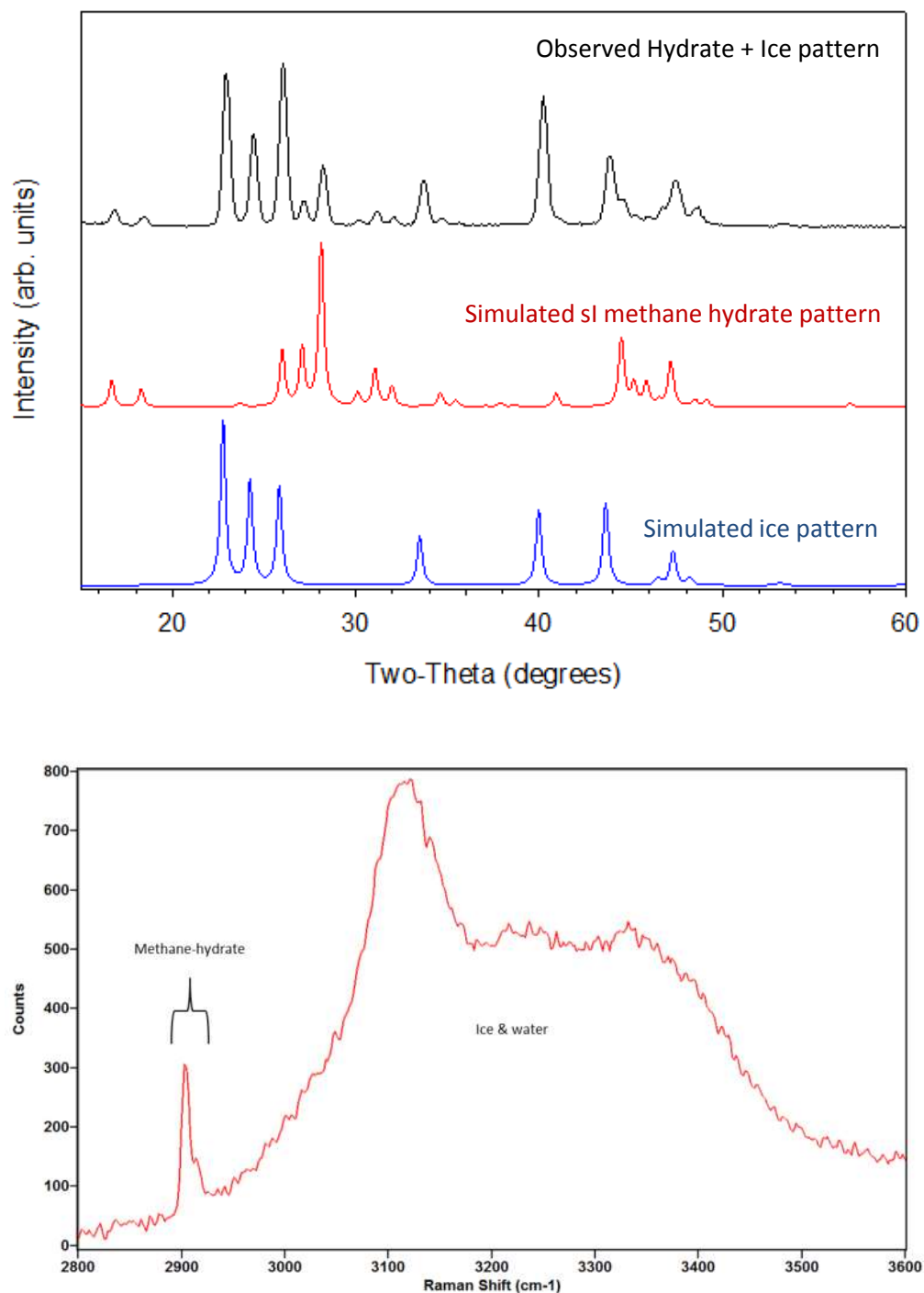
Figure 4-3. Top: Powder X-ray diffraction pattern of methane hydrate grown on ice (black) and calculated powder patterns of sI methane hydrate (red) and ice (blue). Bottom: Raman spectra of methane hydrate on ice sample at 2904 and 2914 cm^{-1}. Large broad bands are from ice and liquid water.

Inclusion of montmorillonite clay surfaces in the reaction vessel has several noticeable effects on the reaction sequence. First, the time required to reach the methane pressure drop from time zero decreases, suggesting that the methane hydrate nucleation period is reduced in the presence of dispersed clay particles. To determine the nucleation period, two tangential trend lines for the constant slope areas before and after the deflection in the pressure-time curve were extended until they crossed. This point we term "the deflection point" which represents the end point of the nucleation period. The elapsed time of the nucleation period and the temperature of the identified pressure at the deflection point were then graphed for each sample (Figure 4-2). Under the investigated conditions, the reduction in the methane hydrate nucleation period is independent of the wt% of the clay in the mixture over the range investigated. At higher loadings of MMT, however, several pressure deflections occur independent of temperature in the region of methane hydrate formation, and will require further investigation to fully evaluate.

4.5. Discussion

Na-Montmorillonite clay is a 2:1 phyllosilicate characterized by layers comprised of two sheets of tetrahedrally-coordinated Si sandwiched about a central sheet of octahedrally-coordinated Al(Mg). Multiple layers are ordered into nanoparticles that have relatively poor crystallinity and limited long range stacking order. SEM analysis of MMT revealed aggregates of clay platelets on the order of 30 nm in size, which was further confirmed by powder XRD and the use of the Scherrer equation to ascertain the average particle size.[39] SWy-2 Na-MMT is known for limited substitution of Mg^{2+} for Al^{3+} in the octahedral sheet. The layer charge requires counter cations in the interlayer spaces. Elemental analysis of the SWy-2 Na-MMT (Table 4-1) shows that a majority of these charge balancing ions are Na^+ [40].

Table 4-1. Composition of SWy-2 Na-MMT

Elemental Analysis [40]	Mass fraction
SiO_2	59.600
Al_2O_3	22.800
Fe_2O_3	47.725
MgO	3.400
CaO	1.140
Na_2O	2.451
K_2O	0.549
TiO_2	0.160
P_2O_5	0.0
MnO	0.036
Cr_2O_3	0.017
S	0.188
Structural formula	
$(Ca_{0.12}Na_{0.32}K_{0.05})[Al_{3.01}Fe(III)_{0.41}Mn_{0.01}Mg_{0.54}Ti_{0.02}][Si_{7.98}Al_{0.02}]O_{20}(OH)_4 \cdot nH_2O$	

Hydrate growth from ice has been postulated to occur first at interstices [6,7]. In the present synthesis of methane hydrate involving the clay-ice mixtures, there are three possible types of interstices: ice-ice, ice-clay, and clay-clay. In this series of experiments, the relative amount of MMT is kept small and is dry-mixed with the pulverized ice. Clay particles are most likely dispersed during mixing, surrounded by ice rather than other clay surfaces. During the warming phase, the primary exposed surface is ice or ice with a layer of water on it with a small fraction of clay surface area.

Adsorption of methane on clay external surfaces and into clay interlayers in the early phase of the reaction must be considered. Adsorption capacity studies examined at similar elevated pressures (6.89 MPa) show relatively high methane adsorption capacities for clays of about 4.3 cm^3/g at 60 °C [41]. The lower temperature in this work will increase the affinity of clay surfaces for methane at these high pressures. Simulations in earlier work have shown the methane-MMT adsorption to be controlled by weak van der Waals-type interactions [42]. In the early reaction phase, methane molecules will be adsorbed to all exposed clay surfaces.

More significantly, the surfaces and interlayers of the clay will attract water. MMT is known to swell taking in 6 cm^3/g of water into the interlayer spaces. Hydration and wetting of MMT clay surfaces depends primarily on the charge balancing counter ions. Unlike Ca^{2+} in other MMT samples, the hydration layer surrounding the smaller low-charge sodium ions in SWy-2 Na-MMT is loosely held. This is of primary importance in the methane hydrate reaction as these less-strongly bound water molecules are available to react with methane to form the hydrate. Simulations have previously revealed that the water-clay interaction is stronger than the methane-clay interaction [42].

The effects of methane adsorption and wettability combine to lower the nucleation time for methane hydrate formation in the presence of SWy-2 Na MMT under the given conditions (Figure 4-2). In the initial warming phase of the reactions, methane is adsorbed onto the exposed external surfaces of MMT and on exposed ice. As the melting point of ice is reached (273 K after approximately 90 minutes), mobile water is now available to associate with the clay surfaces and will displace the methane adsorbed on the clay surfaces. Under the reaction conditions, the adsorbed methane on the ice and clay surfaces and melted ice react quickly to form methane hydrate, indicated by the decrease in methane pressure that occurs less than 31 minutes after the melting point of ice is achieved, at 117 to 119.5 minutes (the longest nucleation) period of any of the clay loaded systems). Without the presence of clay surfaces, methane diffuses into the liquid water phase on the ice particle surfaces to eventually react and form methane hydrate about 50 minutes after the melting point of ice between 141 and 144 minutes. This is an increase of more than 20 minutes in nucleation time to form the methane hydrate compared to the MMT systems under equivalent reaction conditions. Further *in situ* surface studies are underway to better elucidate the fundamentals of the fundamental reaction steps.

4.6. Conclusions

Dispersed montmorillonite particles on ice were shown to decrease the nucleation time by approximately 20 minutes for methane hydrate growth relative to hydrate formation on melting

ice surfaces for our experimental conditions. Experiments using variable clay loading (5, 10, and 15 wt %) with ice show nucleation times of 119 minutes (about 30 minutes after the melting point of ice) for methane hydrate formation. The identical system without clay has a nucleation period of more than 140 minutes (about 50 minutes after the melting point of ice). No further decrease was evident for higher loadings of the clay in these clay-ice mixtures. The presence of the Na-MMT clay surface that adsorbs methane, and which is hydrophilic, serves to facilitate hydrate formation. Further studies to elucidate hydrate growth mechanisms on the clay surfaces using *in situ* spectroscopic monitoring are in progress, along with large-scale molecular dynamics simulations.

4.7. Acknowledgments

4.8. References

[1]   E. D. Sloan and C. Koh, Clathrate Hydrates of Natural Gases, Third Edition, 3rd ed. CRC Press.

[2]   K. A. Kvenvolden and M. A. McMenamin, "Hydrates of Natural Gas: A Review of Their Geologic Occurrence," Geological Survey Circular 825, 1980.

[3]   T. S. Collett, "Natural Gas Hydrates of the Prudhoe Bay and Kuparuk River Area, North Slope, Alaska," AAPG Bull., vol. 77, no. 5, pp. 793-812, 1993.

[4]   T. S. Collett, M. W. Lee, W. F. Agena, J. J. Miller, K. A. Lewis, M. V. Zyrianova, R. Boswell, and T. L. Inks, "Permafrost-associated natural gas hydrate occurrences on the Alaska North Slope," Mar. Pet. Geol., vol. 28, no. 2, pp. 279-294, Feb. 2011.

[5]   K. A. Kvenvolden, "Methane Hydrates and Global Climate," Glob. Biogeochem. Cycles USA, vol. 2:3, Sep. 1989.

[6]   W. F. Kuhs, D. K. Staykova, and A. N. Salamatin, "Formation of Methane Hydrate from Polydisperse Ice Powders," J. Phys. Chem. B, vol. 110, no. 26, pp. 13283-13295, Jul. 2006.

[7]   D. K. Staykova, W. F. Kuhs, A. N. Salamatin, and T. Hansen, "Formation of Porous Gas Hydrates from Ice Powders: Diffraction Experiments and Multistage Model," J. Phys. Chem. B, vol. 107, no. 37, pp. 10299-10311, Sep. 2003.

[8]   L. A. Stern, S. H. Kirby, W. B. Durham, S. Circone, and W. F. Waite, "Laboratory synthesis of pure methane hydrate suitable for measurement of physical properties and decomposition behavior," in Natural Gas Hydrate, Springer, 2003, pp. 323-348.

[9]   S. Takeya, T. Ebinuma, T. Uchida, J. Nagao, and H. Narita, "Self-preservation effect and dissociation rates of CH4 hydrate," J. Cryst. Growth, vol. 237–239, Part 1, pp. 379-382, Apr. 2002.

[10]   Y. Halpern, V. Thieu, R. W. Henning, X. P. Wang, and A. J. Schultz, "Time-resolved in situ neutron diffraction studies of gas hydrate: Transformation of structure II (sII) to structure I (sI)," J. Am. Chem. Soc., vol. 123, no. 51, pp. 12826-12831, Dec. 2001.

[11]   P. S. R. Prasad, V. D. Chari, D. V. S. G. K. Sharma, and S. R. Murthy, "Effect of silica particles on the stability of methane hydrates," Fluid Phase Equilibria, vol. 318, pp. 110-114, Mar. 2012.

[12]   C. V. V. Eswari, B. Raju, V. D. Chari, P. S. R. Prasad, and K. Sain, "Laboratory study of methane hydrate formation kinetics and structural stability in sediments," Mar. Pet. Geol., vol. 58, pp. 199-205, Dec. 2014.

[13]   V. D. Chari, D. V. S. G. K. Sharma, P. S. R. Prasad, and S. R. Murthy, "Methane hydrates formation and dissociation in nano silica suspension," J. Nat. Gas Sci. Eng., vol. 11, pp. 7-11, Mar. 2013.

[14]   V. D. Chari, B. Raju, P. S. R. Prasad, and D. N. Rao, "Methane Hydrates in Spherical Silica Matrix: Optimization of Capillary Water," Energy Fuels, vol. 27, no. 7, pp. 3679-3684, Jul. 2013.

[15]   V. D. Chari, P. S. R. Prasad, and S. R. Murthy, "Structural stability of methane hydrates in porous medium: Raman spectroscopic study," Spectrochim. Acta. A. Mol. Biomol. Spectrosc., vol. 120, pp. 636-641, Feb. 2014.

[16]   K. Lee, S.-H. Lee, and W. Lee, "Stochastic nature of carbon dioxide hydrate induction times in Na-montmorillonite and marine sediment suspensions," Int. J. Greenh. Gas Control, vol. 14, pp. 15–24, May 2013.

[17]   T. Koga, J. Wong, M. K. Endoh, D. Mahajan, C. Gutt, and S. K. Satija, "Hydrate Formation at the Methane/Water Interface on the Molecular Scale," Langmuir, vol. 26, no. 7, pp. 4627-4630, Apr. 2010.

[18]   R. M. Barrer and A. V. J. Edge, "Gas Hydrates Containing Argon, Krypton and Xenon: Kinetics and Energetics of Formation and Equilibria," Proc. R. Soc. Lond. Math. Phys. Eng. Sci., vol. 300, no. 1460, pp. 1-24, Aug. 1967.

[19]   X. Wang, A. J. Schultz, and Y. Halpern, "Kinetics of Methane Hydrate Formation from Polycrystalline Deuterated Ice," J. Phys. Chem. A, vol. 106, no. 32, pp. 7304-7309, Aug. 2002.

[20]   G. Von Froment and K. Bischoff, Chemical Reactor Analysis and Design., 2nd ed. New York: Wiley & Sons, 1990.

[21]   O. Levenspiel, "Chemical Reaction Engineering," Ind. Eng. Chem. Res., vol. 38, no. 11, pp. 4140–4143, Nov. 1999.

[22]   Y. Mizuno and N. Hanafusa, "Studies of Surface-Properties of Ice Using Nuclear-Magnetic-Resonance," J. Phys., vol. 48, no. C–1, pp. 511-517, Mar. 1987.

[23]   G. Genov, W. F. Kuhs, D. K. Staykova, E. Goreshnik, and A. N. Salamatin, "Experimental studies on the formation of porous gas hydrates," Am. Mineral., vol. 89, no. 8–9, pp. 1228-1239, Sep. 2004.

[24]   B. C. Barnes and A. K. Sum, "Advances in molecular simulations of clathrate hydrates," Curr. Opin. Chem. Eng., vol. 2, no. 2, pp. 184-190, May 2013.

[25]   M. B. Clennell, M. Hovland, J. S. Booth, P. Henry, and W. J. Winters, "Formation of natural gas hydrates in marine sediments 1. Conceptual model of gas hydrate growth conditioned by host sediment properties," J. Geophys. Res., vol. 104, no. B10, pp. 22985-23003, Oct. 1999.

[26]   P. Henry, M. Thomas, and M. B. Clennell, "Formation of natural gas hydrates in marine sediments 2. Thermodynamic calculations of stability conditions in porous sediments," J. Geophys. Res., vol. 104, no. B10, pp. 23005-23022, Oct. 1999.

[27]   H. Lu, T. Kawasaki, T. Ukita, I. Moudrakovski, T. Fujii, S. Noguchi, T. Shimada, M. Nakamizu, J. Ripmeester, and C. Ratcliffe, "Particle size effect on the saturation of methane hydrate in sediments – Constrained from experimental results," Mar. Pet. Geol., vol. 28, no. 10, pp. 1801-1805, Nov. 2011.

[28]   M. W. Lee and T. S. Collett, "Unique problems associated with seismic analysis of partially gas-saturated unconsolidated sediments," Mar. Pet. Geol., vol. 26, no. 6, pp. 775-781, Jun. 2009.

[29]   T. Collett, J.-J. Bahk, R. Baker, R. Boswell, D. Divins, M. Frye, D. Goldberg, J. Husebo, C. Koh, M. Malone, M. Morell, G. Myers, C. Shipp, and M. Torres, "Methane Hydrates in Nature-Current Knowledge and Challenges," J. Chem. Eng. Data, vol. 60, no. 2, pp. 319-329, Feb. 2015.

[30]   W. Hao, J. Wang, S. Fan, and W. Hao, "Study on methane hydration process in a semi-continuous stirred tank reactor," Energy Convers. Manag., vol. 48, no. 3, pp. 954-960, Mar. 2007.

[31]   H. K. Abay, T. M. Svartaas, and W. Ke, "Effect of Gas Composition on sII Hydrate Growth Kinetics," Energy Fuels, vol. 25, no. 4, pp. 1335–1341, Apr. 2011.

[32]   S.P. Kang, Y. Seo, and W. Jang, "Kinetics of Methane and Carbon Dioxide Hydrate Formation in Silica Gel Pores," Energy & Fuels, vol. 23, no. 7, pp. 3711-3715, Jul., 2009.

[33]   K. K. Ostergaard, R. Anderson, M. Llamedo, and B. Tohidi, "Hydrate phase equilibria in porous media: effect of pore size and salinity," Terra Nova, vol. 14, no. 5, pp. 307-312, Oct. 2002.

[34]   E. Y. Aladko, Y. A. Dyadin, V. B. Fenelonov, E. G. Larionov, M. S. Mel'gunov, A. Y. Manakov, A. N. Nesterov, and F. V. Zhurko, "Dissociation Conditions of Methane Hydrate in Mesoporous Silica Gels in Wide Ranges of Pressure and Water Content," J. Phys. Chem. B, vol. 108, no. 42, pp. 16540–16547, Oct. 2004.

[35]   D. Riestenberg, O. West, S. Lee, S. McCallum, and T. J. Phelps, "Sediment surface effects on methane hydrate formation and dissociation," Mar. Geol., vol. 198, no. 1–2, pp. 181-190, Jun. 2003.

[36]   Y. Seo, J. Seol, S.-H. Yeon, D.-Y. Koh, M. Cha, S.-P. Kang, Y.-T. Seo, J. Bahk, J. Lee, and H. Lee, "Structural, Mineralogical, and Rheological Properties of Methane Hydrates in Smectite Clays," J. Chem. Eng. Data, vol. 54, no. 4, pp. 1284-1291, Apr. 2009.

[37]   L. A. Stern, S. H. Kirby, W. B. Durham, S. Circone, and W. F. Waite, "Laboratory synthesis of pure methane hydrate suitable for measurement of physical properties and decomposition behavior.," in Natural Gas Hydrate In Oceanic and Permafrost Environments, vol. 5, Dordrecht: Springer Netherlands, 2000, pp. 323-348.

[38]   G. V. P. K. K. R. Ramya, "Raman spectra of vibrational and librational modes in methane clathrate hydrates using density functional theory.," J. Chem. Phys., vol. 136, no. 17, p. 174305, 2012.

[39]   P. Scherrer, "Estimation of the size and structure of colloidal particles by Rontgen rays," Chem. Zentralblatt, no. i, pp. 322-323, 1919 1918.

[40]   H. V. Olphen and J. J. Fripiat, Data Handbook for Clay Materials and Other Non-metallic Minerals, 1st edition. Oxford ; New York: Pergamon Press, 1979.

[41]   D. Liu, P. Yuan, H. Liu, T. Li, D. Tan, W. Yuan, and H. He, "High-pressure adsorption of methane on montmorillonite, kaolinite and illite," Appl. Clay Sci., vol. 85, pp. 25-30, Nov. 2013.

[42]   R. T. Cygan, S. Guggenheim, and A. F. Koster van Groos, "Molecular Models for the Intercalation of Methane Hydrate Complexes in Montmorillonite Clay," J. Phys. Chem. B, vol. 108, no. 39, pp. 15141-15149, Sep. 2004.

5. METHANE HYDRATE SYNTHESIS IN A SPECIALIZED RAMAN CELL

5.1. Abstract

Methane hydrates were synthesized in a Raman spectroscopic cell designed for this purpose. The specialized cell maintains the required pressure and temperature for methane hydrate stability throughout the synthesis and Raman spectroscopic analysis process. This capability is crucial for characterizing temperature- and pressure-sensitive hydrates *in situ*, without exposing these compounds to ambient pressures or temperatures which would affect the methane loading and crystallinity of the materials. Raman spectra collected confirm the presence of methane hydrates. A time-series scan while warming the cell evaluated the melting of remnant ice in the cell followed by methane hydrate decomposition, demonstrating the sensitivity of the instrument and utility of this cell for *in situ* work.

5.2. Introduction

Raman spectroscopy is widely used to characterize hydrate samples in tandem with NMR to determine the hydrate structure (sI, sII, or sH), the cage occupancy (number of methane molecules in the 5^{12} cages, for instance), and completeness of the conversion from ice to hydrate [1,2]. Raman spectroscopy has also been used to compare hydrate stability on various substrates [3-5]. In these previous studies, hydrates were synthesized, cooled to liquid nitrogen temperatures, depressurized, and then transferred to a sample chamber for analysis. In the present work, a specialized high-pressure low-temperature Raman cell was purchased from Aabspec, Inc. to perform spectroscopy of methane hydrate samples grown *in situ* (Figure 5-1). Therefore, no supercooling or depressurization is required to obtain a Raman spectrum. The cell is constructed from a block of stainless steel and fitted with a sapphire window. The end plate is fitted with a cold finger attached to a 4 mm^3 sample cup that opens to the sapphire window. A warming-water circulator is connected to the cell front face to maintain the sapphire window and gaskets at a minimum temperature of 20°C.

Figure 5-1. Raman spectroscopic cell with sapphire window facing outward. Cell is approximately 10 cm wide.

5.3. Experimental Method and Results

The cold finger is precooled to -20°C in a freezer and loaded with gas-free ice. A sub-zero chiller with ethylene glycol is connected to the cold finger and the sample is maintained at less than -5°C during cell assembly and pressurization, as monitored by a continuously-recording thermocouple. The assembled cell is purged and swept with methane three times, then pressurized with methane to 500 psi (3.45 MPa) and isolated from the gas supply cylinder. The cell is allowed to equilibrate for 30 minutes until the pressure is stable. The temperature of the cold finger is then raised until the sample reaches -0.5°C to 0°C. As the result of the small sample size, the efficiency of the cold finger in delivering heat, and the thermal conductivity of the cell, the temperature increase occurs in less than one minute. The cell is maintained at this temperature and pressure near the melting point of ice for the duration of the reaction lasting 12 hours. Reaction path for the synthesis of methane hydrate using the Raman cell is presented in Figure 5-2 along with the higher-pressure path followed in the synthesis with the bulk reaction vessel (see Section 4-3).
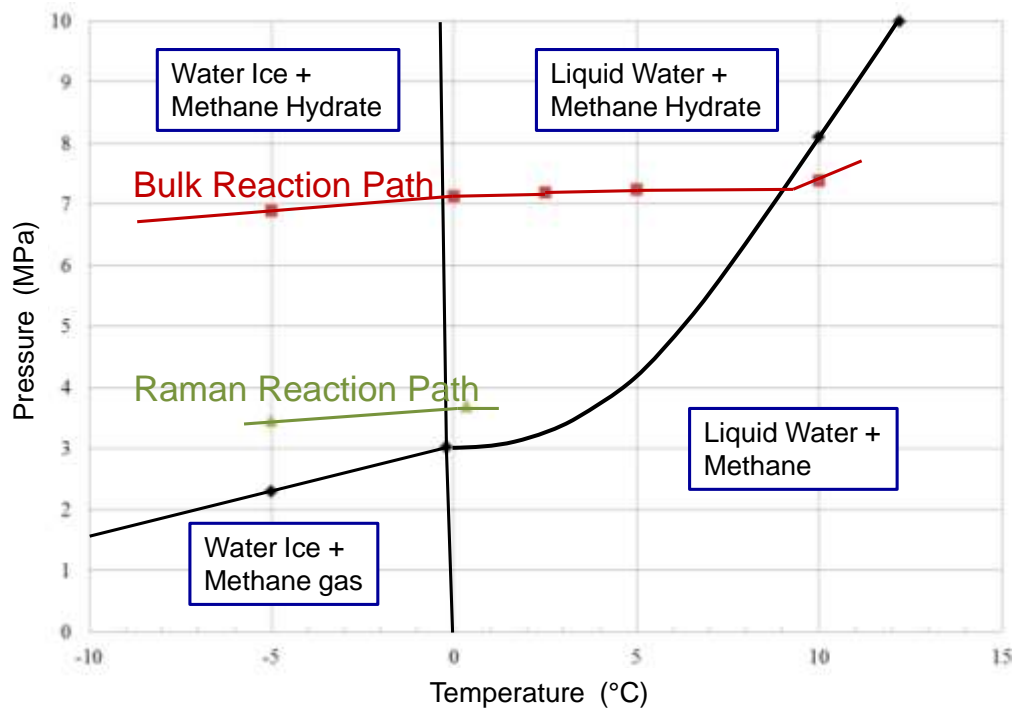
Figure 5-2. Phase diagram with reaction paths for formation and decomposition of methane hydrates synthesized using bulk reaction vessel (red) and spectroscopic Raman cell (green).

A Horiba T64000 Raman Spectrometer fitted with 600 grooves/mm gratings is used for the spectroscopic data collection. A green laser (514.532 nm laser at 50mW at the head and near 21.7 mW into the cell) is used for the excitation of the sample. The instrument is first calibrated by placing a sample of PET in the sample cup and acquiring a spectrum. The Raman cell is then disconnected from the chiller and the water recirculator, and mounted using a custom fabricated stage into the spectrometer and then reconnected to the chiller and recirculator. The sample is maintained at -5°C for the duration of the spectroscopic data collection. The methane hydrate spectrum shown was captured using ten accumulations of ten seconds each (Figure 5-3).
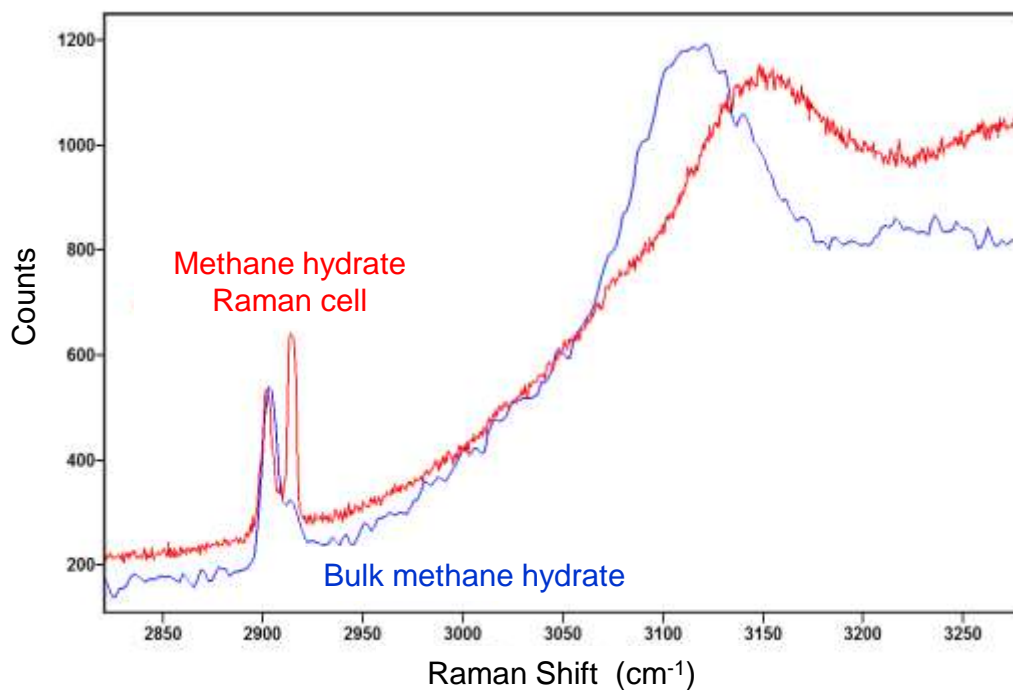
Figure 5-3. Raman spectra for methane hydrate synthesized in the bulk apparatus (blue) and in the spectroscopic Raman cell (red).

The resulting spectra confirm the expected presence of methane hydrate, free methane gas, water, and ice within the Raman cell. The prominent peak at 2915 cm^{-1} for the Raman cell data is the C-H stretch vibration from free methane, while the peak at 2905 cm^{-1} is the C-H stretch of methane in a water cage of methane hydrate. The broad signal above 3100 cm^{-1} arises from water and ice.

The following spectra show the *in situ* decomposition of the methane hydrate sample (Figure 5-4). The chiller temperature was raised, and spectra were taken every thirty seconds for ten minutes until the sample decomposed. For clarity, Figure 5-4 depicts every fourth scan.
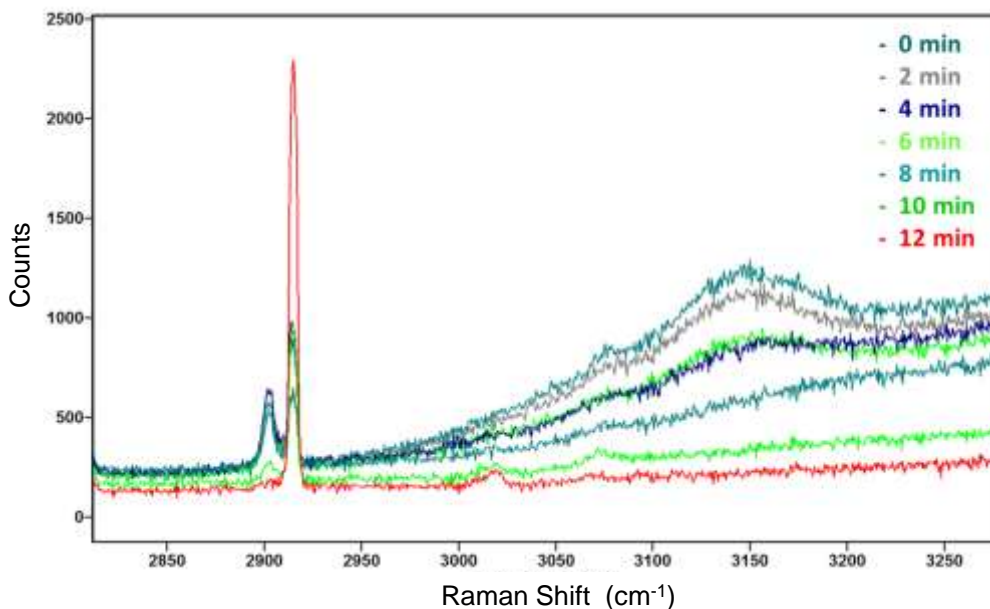
Figure 5-4. Time series data of methane hydrate decomposition in the Raman cell. Depicted frequency scans were collected at two-minute intervals.

Methane hydrate is stable to 8°C; in the decomposition experiment, the broad signal above 3100 cm^{-1} owing to ice and water begins to fade after four minutes and is completely gone after eight minutes. The sample cup is open horizontally to the sapphire window and the Raman laser. As the ice melts, water leaks out of the sample cup and out of the laser beam. The methane hydrate persists until the scan at ten minutes, as shown by the signal at 2905 cm^{-1}. The remaining peak in the final scan (red) at twelve minutes is due to free methane present in the cell (still under pressure).

5.4. References

[1]   R. Susilo, J. A. Ripmeester, and P. Englezos, "Characterization of gas hydrates with PXRD, DSC, NMR, and Raman spectroscopy," *Chem. Eng. Sci.*, vol. 62, no. 15, pp. 3930–3939, 2007.

[2]   G. V. P. K. K R Ramya, "Raman spectra of vibrational and librational modes in methane clathrate hydrates using density functional theory," *J. Chem. Phys.*, vol. 136, no. 17, p. 174305, 2012.

[3]   V. D. Chari, P. S. R. Prasad, and S. R. Murthy, "Structural stability of methane hydrates in porous medium: Raman spectroscopic study," *Spectrochim. Acta. A. Mol. Biomol. Spectrosc.*, vol. 120, pp. 636–641, 2014.

[4]   V. D. Chari, B. Raju, P. S. R. Prasad, and D. N. Rao, "Methane hydrates in spherical silica matrix: Optimization of capillary water," *Energy Fuels*, vol. 27, no. 7, pp. 3679–3684, 2013.

[5]   P. S. R. Prasad, V. D. Chari, D. V. S. G. K. Sharma, and S. R. Murthy, "Effect of silica particles on the stability of methane hydrates," *Fluid Phase Equilibria*, vol. 318, pp. 110–114, 2012.

6. WEAK INTERACTIONS BETWEEN WATER AND CLATHRATE-FORMING GASES AT LOW PRESSURES

6.1. Abstract

Using scanning probe microscopy and temperature programed desorption we examined the interaction between water and two common clathrate-forming gases, methane and isobutane, at low temperature and low pressure. Water co-deposited with up to 10^{-1} mbar methane or 10^{-5} mbar isobutane at 140 K onto a Pt(111) substrate yielded pure crystalline ice, i.e., the exposure to up to ~10^7 gas molecules for each deposited water molecule did not have any detectable effect on the growing films. Exposing metastable, less than 2 molecular layers thick, water films to 10^{-5} mbar methane does not alter their morphology, suggesting that the presence of the Pt(111) surface is not a strong driver for hydrate formation. This weak water–gas interaction at low pressures is supported by our thermal desorption measurements from amorphous solid water and crystalline ice where 1 ML of methane desorbs near ~43 K and isobutane desorbs near ~100 K. Similar desorption temperatures were observed for desorption from amorphous solid water.

6.2. Introduction

Owing to their large natural abundance(s), often at the same location, the interaction between hydrocarbons and water plays an important role in various geochemical and astrochemical settings. Most importantly, some gaseous hydrocarbons like methane combine at low temperatures and elevated pressures with water to form clathrates, i.e., solid hydrates consisting of individual gas molecules surrounded by cages of hydrogen-bonded water molecules [1]. Clathrate deposits have been found in large quantities on the outer continental shelf and in permafrost environments [1-3] and are believed to occur in numerous astrophysical environments [4-7]. The prospect of exploiting them as energy sources but also incidents of pipeline blockages by clathrates and the danger from potential releases of large quantities of methane, a potent greenhouse gas, have fueled extensive research aimed at understanding the interaction between water and hydrate-forming natural gases (henceforth "HFNG"). Various research groups have synthesized natural gas clathrates under laboratory conditions that mimic geological [1,8-11] or astrophysical [5,6,12-14] environments yielding valuable information about thermal properties and bulk phase equilibria.

However, experiments that probe molecular-level amounts of material [15-17] are scarce, and microscopy data are only available down to the micron scale [9,14]. Thus, there is little direct experimental support for modeling efforts [18-24] to understand how HFNGs interact with water at the molecular scale. Under conditions at which natural clathrates are typically found on earth, i.e., temperatures between 250 K and 300 K and pressures on the order of 100 bar [1,25], hydrate formation occurs much too fast to be observable with molecular-layer resolution. To achieve such sensitivity, experiments must be conducted at much lower pressure and temperature. In this work we employ an ultrahigh vacuum (UHV) environment to control the amount of examined material with molecular-layer accuracy. We deposit water and HFNGs onto an atomically flat Pt(111) substrate and monitor their interaction using two surface science techniques with sub-molecular layer resolution, scanning tunneling microscopy (STM) and temperature programmed desorption (TPD).

The experimental conditions are chosen with two goals in mind. The first is to increase the likelihood of forming clathrates or precursors thereof, or at least, get as close as possible to clathrate stability, by reducing temperature and increasing gas pressure. The second goal is to adjust the thermal mobility of water molecules such that mass transport involving crystalline ice or clathrates occurs at a rate that permits molecular-layer resolved monitoring. For water molecules, in order to arrange themselves into ordered structures, i.e., the crystal lattice of ice or hydrate cages, they have to be able to break and reform hydrogen bonds at a sufficient rate. Judging from measured rates of bulk diffusion [26] and surface diffusion [27] of ice, the lowest temperature at which formation of crystalline clathrates is expected to occur at a convenient time scale is ≈140 K. We thus deposit the films for our STM experiments at ≈140 K.

We chose methane for our study because it is by far the most abundant clathrate-forming hydrocarbon. Isobutane was selected because it is also rather common, accounting for ≈1% of the clathrates found in the Earth's oceans, and because its hydrate requires a significantly lower pressure to be stabilized than methane clathrate [1]. Perhaps due to a recent focus mostly on terrestrial hydrates, there are only few data available for the methane/water system below 230 K, and, apparently none for isobutane/water. Fray and coworkers [6] compiled an equilibrium-pressure curve of methane clathrate as a function of temperature based on their own measurements and those of Delsemme and Wenger [5], Falabella and Vanpee [12], and others. Extrapolating this curve to $T = 140$ K suggests that a methane pressure of ≈15 mbar is needed to stabilize the bulk phase of methane clathrate. According to Sloan and coworkers' compiled data presented in Ref. [1], the hydrate-forming pressure at the lowest temperature for which data are available is ~50 times lower for isobutane (~0.18 bar at 242 K, [1,28]) than for methane (~9 bar at 242 K). If this pressure ratio is similar at $T = 140$ K, the optimum temperature for our UHV experiments, one would need ≈0.3 mbar of isobutane to stabilize the bulk hydrate phase, a pressure that is still excessively high for operating UHV setups.

However, at these low temperatures, clathrates might be able to exist also outside their bulk-stability region as a metastable bulk phase (like amorphous solid water that persists, or cubic ice that persists and even forms at 140 K [29,30]). In addition, clathrates might have an extended stability region near interfaces, the same way as, for example, water pentagon-hexagon-heptagon arrangements represent the equilibrium configuration in the 2D wetting layer of water on Pt(111) [31,32], Ni(111)[33], Pd(111), and Ru(0001) [34], despite not being stable in the bulk at any pressure or temperature. That interfaces could promote the formation of methane clathrates had recently been suggested by Pirzadeh and Kusalik [24] for the case of an ice-solution interface.

Guided by the considerations above we explored various kinetic pathways to promote a strong HFNG-water interaction. Besides co-deposition of water with methane or isobutane, we also grew HFNG and water layers sequentially followed by annealing to ≈140 K. Most experiments resulted in ice layers without clear evidence that the presence of the HFNGs had any effect on film structure and morphology. However, when first growing a saturated isobutane monolayer followed by 2-3 molecular layers of water, a film with smooth and clustered regions developed. This morphology, very distinct from that of pure water films, could either indicate formation of a 2D hydrate layer or be the result of water dewetting facilitated by the presence of isobutane.

6.3. Experimental methods

6.3.1. Scanning tunneling microscopy experiments

For the STM experiments, we prepared and analyzed the film samples in a UHV chamber with a base pressure of $< 3 \times 10^{-11}$ mbar. Water was deposited at a rate of ≈1 Å/min by directing water vapor onto an atomically flat Pt(111) surface held at 140 K. For gas exposure the UHV chamber was backfilled using standard UHV leak valves. During most co-deposition experiments the water deposition rate was maintained by monitoring the $m/z = 18$ peak with a mass spectrometer, while gas exposure was controlled with an ion gauge measuring the total chamber pressure. During film growth, the STM tip was retracted far from the sample to exclude tip-induced modifications of the films. STM measurements were performed at T < 110 K using tunnel currents below 1 pA. To image films thicker than 1 nm non-destructively [35,36] we applied a sample bias of ≈ -6 V.

For gas exposures above 10^{-5} mbar all high voltages in the UHV chamber, including ion gauge and mass spectrometer, were turned off. The integrity of the vacuum was maintained by two turbo pumps operating through partially closed valves. The chamber pressure, between 10^{-3} and 1 mbar, was measured with a convectron gauge calibrated for methane, and above 1 mbar, a Heise pressure transducer was used. Condensation of significant amounts of gas onto the coldest parts in the UHV chamber ultimately limited the maximum gas pressures we could apply. In the case of methane, release of condensation heat and possibly increased heat loss via thermal conduction through the methane gas limited the maximum methane pressure to 0.1 mbar. At higher pressures the sample temperature and the methane pressure could not be controlled simultaneously. In the case of isobutane, the maximum pressure for well-controlled experiments was ~10^{-5} mbar. At higher pressures, significant amounts of isobutane desorbed from cold surfaces of the cooling system and re-adsorbed on the sample surface when cooling the sample below 110 K for STM measurements.

6.3.2. Thermal desorption experiments

The TPD experiments were conducted at PNNL in a UHV chamber with a base pressure of $< 1 \times 10^{-10}$ mbar which has been described in detail elsewhere [37,38]. Briefly, the substrate was a 1 cm diameter by 1 mm thick Pt(111) single crystal that was spot-welded on the back side to tantalum leads for resistive heating. A K-type thermocouple spot-welded to the back of the Pt(111) substrate was used to measure temperature with a precision of better than ± 0.01 K and an estimated absolute accuracy of ± 2 K. The Pt(111) was cleaned using Ne$^+$ sputtering, oxygen anneal, and temperature annealing previously described [38]. The substrate was cooled using a closed cycle helium cryostat that could achieve a base temperature of ~25 K.

Water films were deposited using a quasi-effusive molecular beam collimated by three stages of differential pumping at normal incidence to the Pt(111) substrate. Water was deposited at a rate of 0.87 ML/s, where 1 ML is defined as the monolayer saturation coverage on the Pt(111) substrate and corresponds to ~1.1×10^{15} molecules/cm^2 [39]. The HFNGs were deposited at normal incidence using a separate quasi-effusive molecular beam collimated by four stages of differential pumping. The coverages of the HFNGs were defined by their monolayer saturation

coverages on Pt(111). The ML areal coverage (#/cm^2) can be estimated by converting the liquid density (0.422 g/cm^3 for CH$_4$ and 0.594 g/cm^3 for isobutane) to a number density (molecules/cm^3) and taking the 2/3 root. This procedure yields a ML density of 6.3 $\times 10^{14}$molecules/ cm^2 for methane and 3.4×10^{14} molecules/cm^2 for isobutane. Desorption spectra were obtained with an Extrel quadrupole mass spectrometer in a line-of-sight configuration. Methane desorption was monitored at $m/z = 15$ and $m/z = 43$ was utilized for isobutane desorption. A linear heating rate of 1 K/s was used for all of the TPD experiments.

6.4.   Results and discussion

6.4.1. The interaction of water and methane

6.4.1.1.   Co-deposition of water and methane

The first experiment to probe water-methane interaction was performed via co-deposition of water and methane onto a well-cleaned Pt(111) single-crystal substrate held at 140 K. The sample surface was simultaneously exposed for 8 min to $p_{water} = 5 \times 10^{-9}$ mbar partial pressure of water and a partial pressure of $p_{meth}=10^{-5}$ mbar methane. The choice of $p_{meth} = 10^{-5}$ mbar is dictated by the maximum pressure at which water deposition could be controlled precisely (via mass spectrometer) and the integrity of the ultrahigh vacuum could be fully maintained (via a turbo pump). Except for the added exposure to methane all experimental conditions, i.e., sample temperature, partial pressure of water, and exposure time were chosen to match those that had previously [35,36] been used to grow 2-3 nm high crystallites of ice Ih embedded in a 1-molecule thin wetting layer. Fig. 6-1(a) shows the unambiguous result: a film evolved that is indistinguishable from ice films grown in the absence of methane. (For comparison see Fig. 3(c) in Ref. [35] and Fig. 1 in [36]). From this close match in morphology we infer that the film grown via co-deposition also consists of pure water ice and not hydrate. This inference is based on the common observation that film morphologies, e.g., the aspect ratio of crystals, are very sensitive to changes in energetic and kinetic parameters. For example, small variations in growth conditions of water/Pt(111) (compare Refs. [40] and [41] with Refs. [36] and [42]), or substituting the Pt(111) substrate with Ni(111) [33] lead to dramatic changes in film morphology, i.e., the aspect ratio of isolated crystallites and the mean film thickness at coalescence. We thus assume that substituting water ice with gas hydrate as the film material would result in an obvious change in morphology, inconsistent with what we observe.

For the following co-deposition experiment we increased the methane pressure to the maximum value $p_{meth} = 0.1$ mbar at which both the sample temperature and the methane pressure could still be reasonably well controlled. (Condensation of methane onto the cooling assembly caused the sample to heat up, which had to be compensated by increasing the flow of the liquid He cooling fluid. Resulting variations in methane condensation led to methane pressure changes, which then had to be compensated by adjusting the methane dose.) The temperature excursions were smaller than $\pm$ 5 K, and the methane pressure was maintained with an accuracy of ~50%. In this experiment we deposited water for a longer time, 15 min, to reduce the relative impact of the inaccuracy of the deposition amounts during the initial phase of co-deposition.[1] After co-depositing water at $p_{water} = 5 \times 10^{-9}$ mbar and methane at $p_{meth} = 0.1$ mbar for $\approx$ 15 min onto the

Pt sample held at 140 K, water dosing was stopped while exposure to 0.1 mbar methane was continued for 5 more min before the sample was cooled down for imaging.

The resulting film is depicted in Fig. 6-1(b) and at higher magnification in Fig. 6-1(c). This snake-like morphology is characteristic of the early stage of coalescence during the growth of crystalline ice films. The morphology is strikingly similar to that of an ice film grown under similar conditions but without methane, shown in Fig. 3(d) of Ref. [35]. There are two differences, though. First, the lateral scale of the features in the co-deposited film are smaller, presumably due to reduced water diffusion, which might have been caused by a slightly lower sample temperature or by the presence of the methane. The second difference from the pure water experiment in Ref. [35] is that the film surface is not molecularly flat. The slightly rounded shapes in Fig. 6-1(b,c) are most certainly produced by 'post-growth' residual material that adsorbed onto the film after quenching the sample to the imaging temperature, because the chamber pressure recovered only very slowly from dosing methane at 0.1 mbar. (Three hours after film deposition the chamber pressure was still 4×10^{-4} mbar). But the average height of the crystallites at coalescence, a value very sensitive to surface, interface, and surface-step energies, and therefore highly dependent on the film material, is identical (≈ 2 nm) within experimental error. As in the previous experiment discussed above, this close match in morphology leads us to infer that the film grown via co-deposition also consists of pure water ice and not hydrate. Thus, the simultaneous exposure to approximately 10^7! methane molecules for each deposited water molecule has no obvious effect on the formation of an ice film, except, possibly, a small reduction in water surface diffusion!

[1]The co-deposition experiment with $p_{meth} = 0.1$ mbar required an initialization period of ≈ 5 min during which stable pumping and water and methane dosing had to be established: First, water dosing was initialized and deemed stabilized when the mass spectrometer signal of p_{water} varied by less than $\approx 10\%$ / min without regulating the water dosing valve. Then, the ion gauge and mass spectrometer were shut off and the methane exposure was ramped up to 0.1 mbar, simultaneously adjusting the sample cooling to maintain a sample temperature of 140 K $\pm$ 5 K.
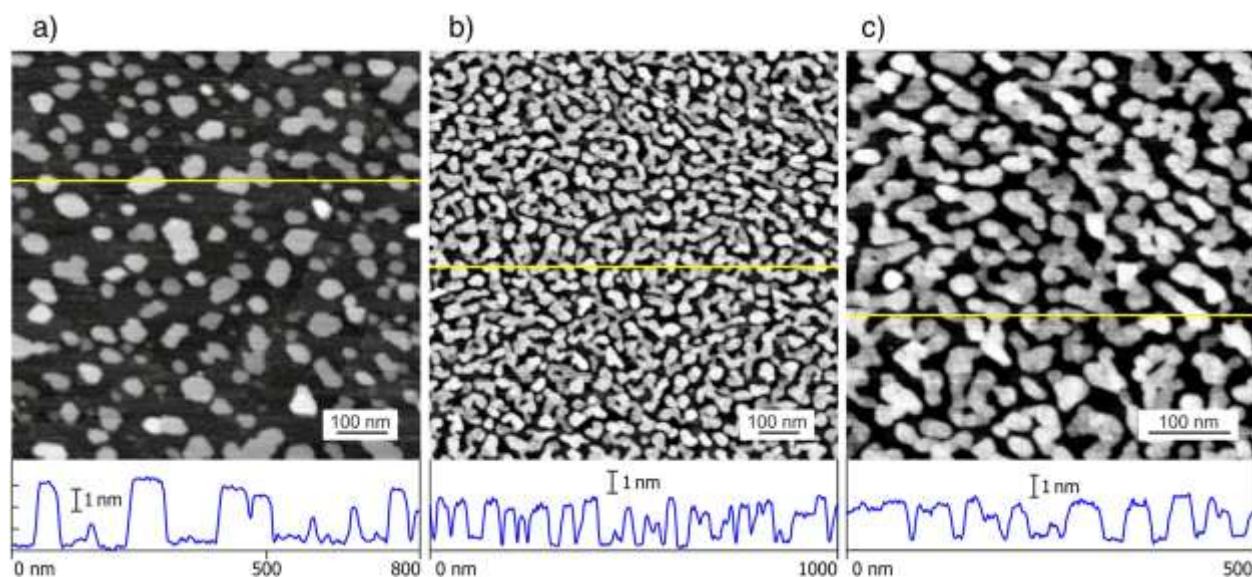
Figure 6-1. Co-deposition of water and methane. (a) 800 nm × 800 nm STM image of Pt(111) after 8 min simultaneous exposure at 140 K to 5×10^{-9} mbar water and 10^{-5} mbar of methane. (b,c) STM images of a film grown via 15 min co-deposition of 5×10^{-9} mbar water and 0.1 mbar of methane. Fields of view are 1 μm^2 and 500 nm × 500 nm, respectively. None of the images reveal any evidence of clathrate formation; pure water-ice films evolved instead.

6.4.1.2. Sequential deposition of water and methane

To probe whether the presence of the Pt(111) substrate enhances the water–methane interaction, very thin metastable water films were subjected to methane exposure. First a water film of ≈ 2 molecular layers (ML) thickness was grown by exposing the Pt(111) surface held at 145 K to 2×10^{-9} mbar water for 90 s. The resulting film, shown in Fig. 6-2(a), is comprised of 2 to 3 ML thick patches (bright) embedded in a 1 ML thick wetting layer (black). This configuration is metastable because a water film of the same thickness in equilibrium consists of much taller 3D crystallites embedded in a 1 ML-thick wetting layer [43,35]. Exposing this configuration to 10^{-5} mbar methane does not cause any discernable change in the film morphology (Fig. 6-2(b)), revealing that the close proximity of the interface with the Pt(111) crystal does not tip the phase balance towards hydrate formation. A similar experiment was performed by first growing a 1 nm thick metastable amorphous solid water (ASW, "amorphous ice") film at 110 K, and subsequently annealing this film in a methane atmosphere of 10^{-7} mbar at 145 K for 10min. Again, exposure to methane did not cause any detectable change in film morphology (not shown).
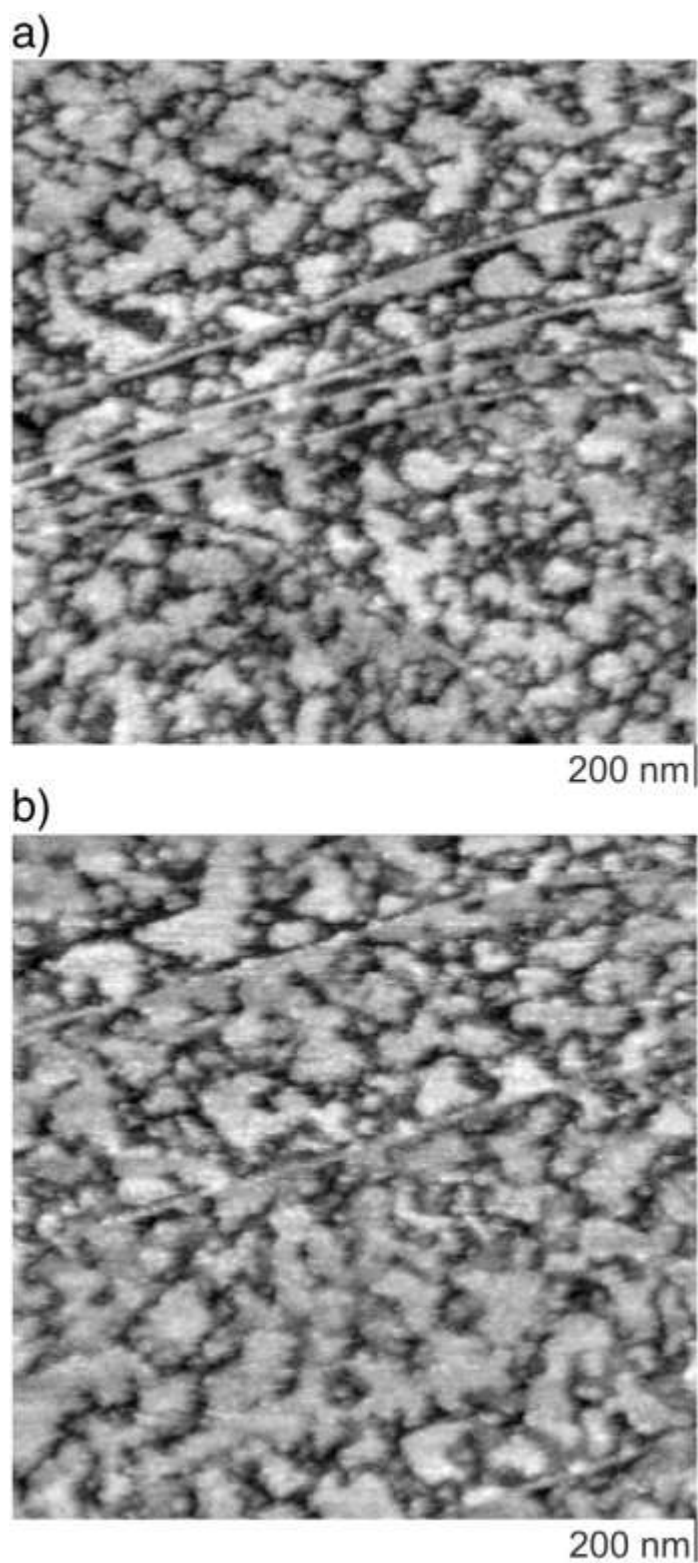
Figure 6-2. 200 nm× 200 nm STM images of a metastable 2ML-thickwater/Pt(111) film grown at 145 K (a) before, and (b) after a 10 min exposure to 10^{-5} mbar of methane, revealing that exposure to methane did not modify the film.

6.4.1.3. Thermal desorption experiments of the water/methane system

The above STM experiments clearly show that neither the co- nor sequential-deposition of methane has an effect on the morphology of vapor deposited water films. These results suggest that the methane-water interaction is too weak to affect changes in the water structure. To gain quantitative insight into the energetics of the methane-water interaction we now examine how a ML of methane desorbs from water substrates (for TPD measurements involving higher methane coverages see supplementary material Fig. S1). Fig. 6-3 displays the TPD spectra for 1 ML of methane deposited on a 100 ML thick ASW film (red curve), on a 100 ML thick crystalline ice (CI) film (blue curve), and on bare Pt(111) (green curve). The ASW film was initially deposited at 30 K and then heated to 80 K to remove some of the film's surface microporosity [38]. The spectra show that methane on either ASW or CI desorbs at a much lower temperature than on Pt(111) but the difference between ASW and CI is small. A rough estimate of the binding energy can be obtained from the Polanyi-Wigner equation [44] using the peak temperature, peak desorption rate, peak coverage, and assuming first-order desorption kinetics. A prefactor of 10^{13} s^{-1} has been experimentally determined for methane desorption from MgO(100), C(0001)/Pt(111), and Pt(111) [45] and was used in the calculations for methane. This calculation yields binding energies of 11.0, 11.2, and 16.7 kJ/mol for methane on ASW, CI, and Pt(111) respectively. It is interesting to note that the methane binding energies on ASW and CI are much lower than the hydrogen bond energy of 29.5 kJ/mole in crystalline ice [46] and the sublimation energy of ~55 kJ/mol for multilayer ASW and crystalline ice [47]. These results are consistent with the STM observations that methane does not affect the ice layer structure. Obviously, a more rigorous analysis is needed to obtain more accurate binding energies, but these estimates do provide a qualitative basis for comparison.

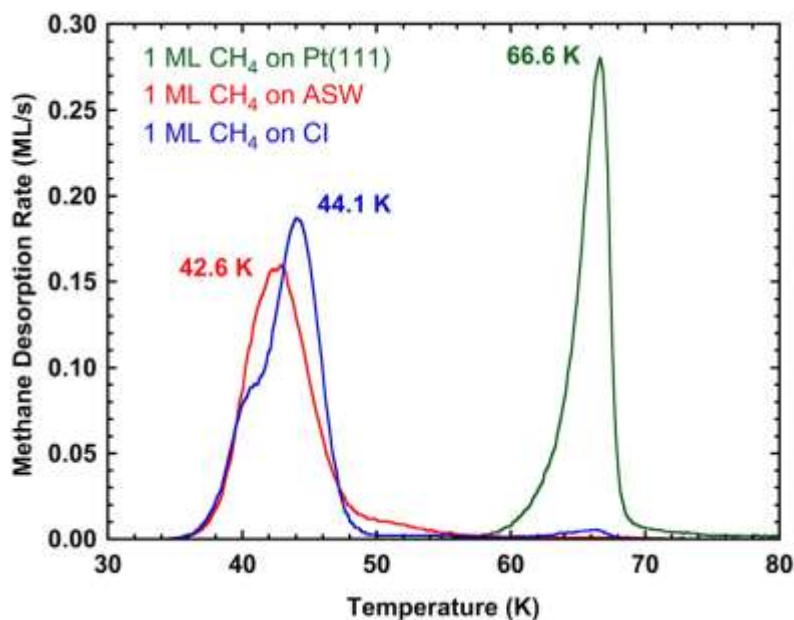
Figure 6-3. TPD spectra for 1 ML of methane deposited on a 100 ML thick ASWfilm (red curve), on a 100 ML thick crystalline ice film (blue curve), and on bare Pt(111) (green curve). Methane was deposited at 25 K and the heating rate was 1 K/s.

Experiments where methane was deposited underneath of ASW overlayers were also conducted. An example is displayed in Fig. 6-4(a) where 25 ML ASW was deposited on top of 1 ML of methane at 30 K. The methane desorption (black curve) is delayed until about 159 K and occurs at a "bump" in the water desorption spectrum (blue curve). The "bump" is the result of the higher free energy (higher vapor pressure) amorphous phase transforming to the lower free energy (lower vapor pressure) crystalline phase. The abrupt desorption of the gas underlayer during crystallization of ASW has been observed before and has been called the "molecular volcano" [48,16]. The abrupt desorption of gases from underneath of ASW films is caused by cracks that form during the crystallization of the ASW overlayer. Fig. 6-4(b) displays TPD spectra for 1 ML of methane underneath of ASW overlayers of 25, 50, 100, and 200 ML. The corresponding water spectra are left off here for clarity but are shown in the supplementary material as Fig. S2. There are two sets of peaks, those between 155 and 160 K labeled "volcano peaks" and those between 170 and 185 K labeled "trapped peaks". Crystallization-induced crack formation begins at the vacuum interface and moves into the film and as a result the "volcano" peak moves to higher temperature with increasing overlayer thickness [16,49,17]. At some thickness the cracks do not span the entire film and the underlying methane remains "trapped" in the film until the water overlayer itself desorbs. The amount of methane that desorbs in the "volcano" peak is nearly 100% for the smallest overlayer thickness (25 ML) but then decreases with increasing overlayer thickness. The temperature for crystallization of the entire film is a function of film thickness and is complete at a temperature just after the volcano peak. Methane that does not desorb in the "volcano" peak remains trapped in the crystallized water film and desorbs when the water layer itself desorbs. For very thick ASW overlayers (> 300 ML, not shown) nearly 100% of the methane desorption occurs in a "trapped" peak. The observations here are the same as those for other gases (N_2, O_2, Ar, Kr, Xe, etc.) [16,17,48-50]. This result also supports the idea that methane does not affect the ASW structure.
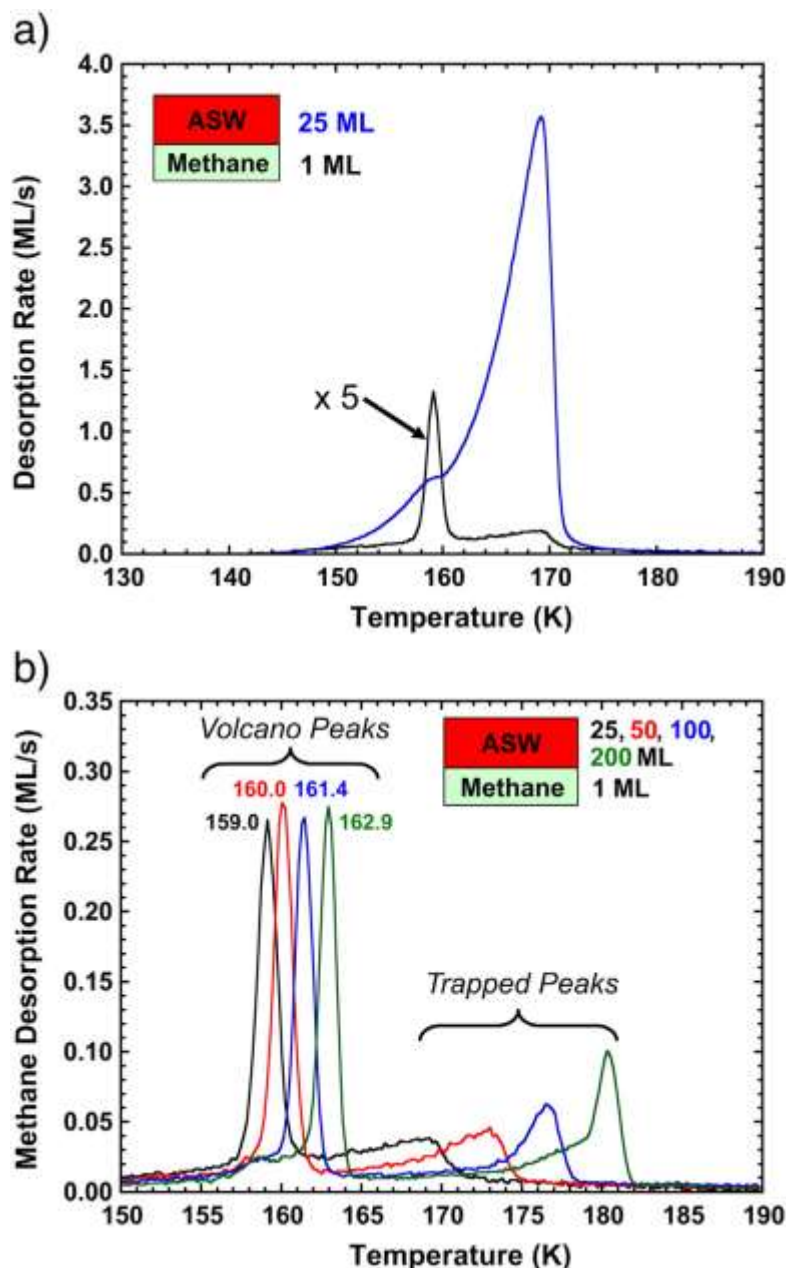
Figure 6-4. TPD spectra of 1 ML of methane buried underneath ASW. (a) TPD spectra for 25 ML of water deposited on top of 1 ML of methane at 30 K and heated at 1 K/s. The methane desorption (black curve) is delayed until about 159 K and occurs at a "bump" in the water desorption spectrum (blue curve). The methane signal is multiplied by a factor of 5. (b) TPD spectra for 1 ML of methane deposited underneath of ASW thicknesses of 25 (black), 50 (red), 100 (blue), and 200 ML (green). Methane and water were deposited at 30 K and the heating rate was 1 K/s. The peaks between 155 and 165 K labeled as "volcano peaks" are due to methane desorption that occurs during ASW crystallization. The "volcano" peak shifts to higher temperature with increasing overlayer thickness. The peaks between 170 and 185 K are labeled as "trapped peaks" and are due to methane desorption that occurs during desorption of the ASW overlayer.

6.4.2. The interaction of water and isobutane

6.4.2.1. Co-deposition of water and isobutane

We also investigated the influence of isobutane on the growth of thin water films. Isobutane is a hydrocarbon that forms hydrates at a significantly lower pressure than methane [1]. Xu et al. [51] reported that isobutane, deposited at T ≤ 140 K onto Pt(111), condenses into a 1-molecule thick 2D layer. To facilitate water-isobutane interaction, we first grew such a monolayer of isobutane at 120 K by exposing the Pt(111) surface for 2 min to 5×10^{-8} mbar isobutane. We then raised the sample temperature to 140 K for an 8 min co-deposition of 5×10^{-9} mbar water and 5×10^{-8} mbar isobutane. The parameters of water deposition were chosen such that, in the absence of isobutane, regularly-shaped 3D ice crystals would emerge [35,36]. The sample was then cooled down below 120 K for imaging. The resulting film is shown in Fig. 6-5(a): The 2-3 nm high azimuthally aligned hexagonal prisms exactly match the morphology of 3D ice crystals that form without any exposure to isobutane [35,36]. As in the case of co-deposited methane (see Section 6.4.1.1) we infer that the film consists of water-ice crystals. In another experiment the isobutane pressure was increased to the maximum value at which well-controlled experiments could still be performed, 10^{-5} mbar. (At higher isobutane pressures large quantities of isobutane condense onto the cold surfaces of the cooling assembly generating a substantial isobutane reservoir inside the UHV chamber. Isobutane desorbing from this reservoir can re-adsorb onto the sample when it is cooled below 120 K for imaging.) Fig. 6-5(b) shows a film grown by 8 min co-deposition of 5×10^{-9} mbar water and 10^{-5} mbar isobutane. This significant increase of isobutane pressure had no discernable effect on the resulting film. Hence, an isobutane pressure of 10^{-5} mbar turned out to be still too low to produce hydrates, and pure ice crystals formed instead.

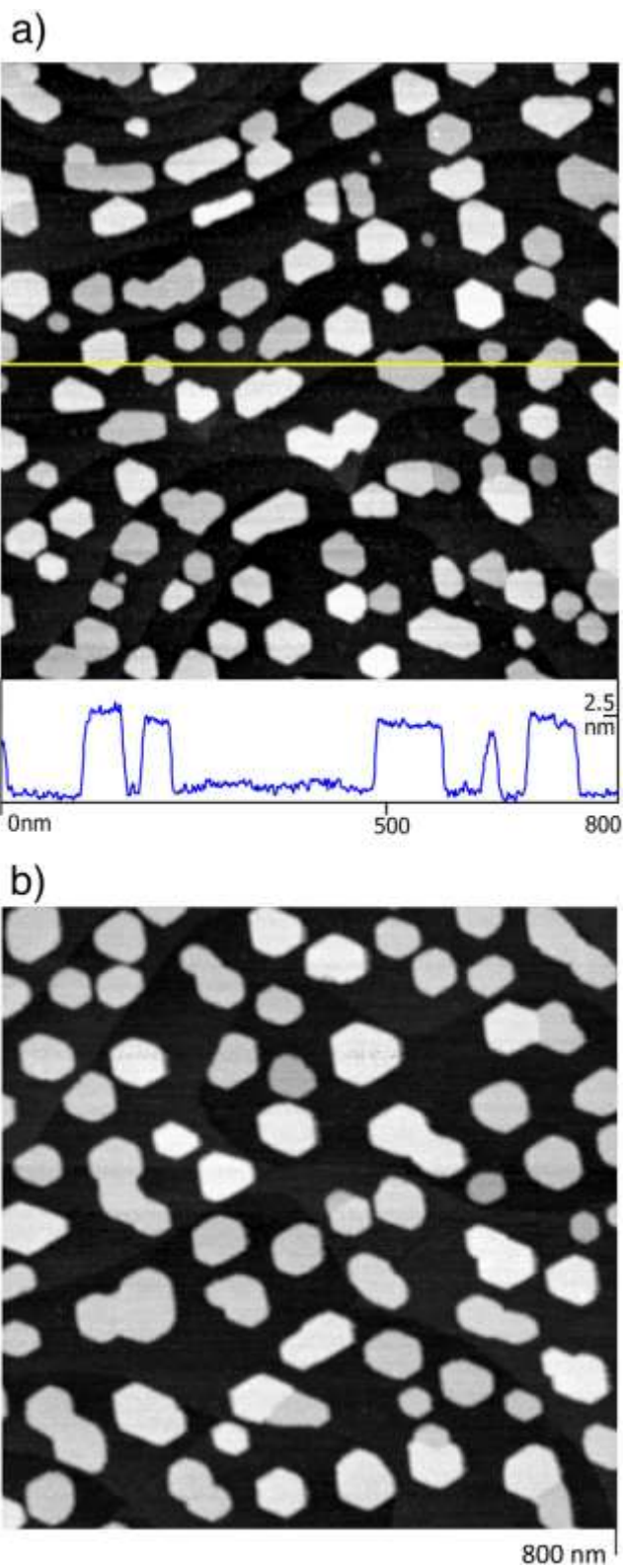**Figure 6-5.** STM images of films produced by 8 min co-deposition of 5×10^{-9} mbar water at 140 K with (a) 5×10^{-8} mbar isobutane, and (b) 10^{-5} mbar isobutane. The film in (a) was grown onto a previously deposited molecular layer of isobutane.

6.4.2.2.   Sequential deposition of water and isobutane

To test whether the presence of the Pt(111) substrate enhances the water-isobutane interaction, we sequentially grew very thin films of both materials on top of each other. The fact that isobutane sticks to Pt(111) at 140 K allows us to cap an isobutane monolayer with two molecular layers of water: Guided by Xu et al. [51] a saturated monolayer of isobutane was grown at 140 K by exposing the Pt(111) surface for 2 min to 5×10^{-8} mbar isobutane. As seen in the STM images in Fig. 6-6(a,b), isobutane forms a complete layer and does not cluster. (The main features apparent in Fig. 6-6(a) are the atomic Pt(111) steps. Zooming into a substrate terrace (Fig. 6-6(b) reveals some structure of the isobutane layer, e.g., a STM tip induced hole.) Subsequent deposition at 140 K of 2-3 molecular layers of water on top of the isobutane led to a morphology that is approximately evenly divided into smooth and clustered regions, shown in Fig. 6-6(c). Annealing the sample to 150 K had no discernable effect.

Are the clustered regions in Fig. 6-6(c) composed of clathrates or clathrate precursors? Fig. 6-6(a,b) had already shown that isobutane by itself does not cluster. But could the isobutane have first migrated to the surface and then formed clusters on top of the water? Or does a 2–3 ML thick water film cluster, with or without the help of isobutane? To elucidate these questions a separate experiment was performed in which the order of deposition was reversed.

As shown in Fig. 6-6(d), pure 2-3ML thick water forms a complete and rather homogeneous film. In other words, in the absence of isobutane, water (of that thickness) does not cluster. Exposing this film to 6 Langmuir (5×10^{-8} mbar for 2 min) of isobutane does not alter the surface (see Fig. 6-6(e)), eliminating the possibility of isobutane clustering when located above the water. Hence there are two remaining straightforward explanations for the clustering in Fig. 6-6(c): the presence of the Pt(111) substrate promotes the formation of a hydrate, or the presence of isobutane facilitates dewetting and clustering of water. Lacking a method with chemical sensitivity, like infrared adsorption spectroscopy (IRAS), the nature of the clusters in Fig. 6-6(c) could not be determined with certainty.
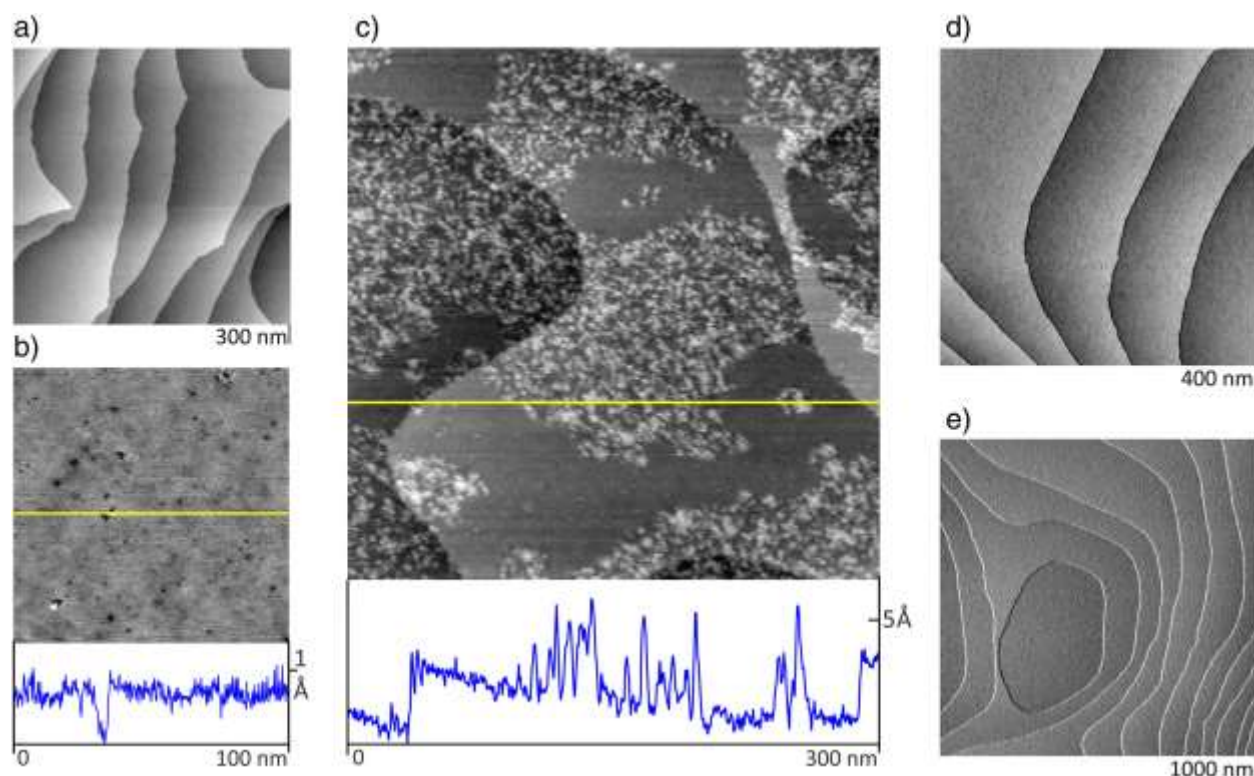
Figure 6-6. Sequential deposition of water and isobutane. (a,b) STM images of a saturated isobutane monolayer deposited onto Pt(111) at 140 K. The profile at the bottom was taken along the yellow line in (b). (c) STM image of a saturated isobutane monolayer deposited onto Pt(111) at 140 K, subsequently covered up by 2-3 molecular layers of water. (d,e) STM images of (d) 2 ML of water deposited onto Pt(111) at 140 K, and (e) after the film of (d) has been exposed at 130 K for 2min to 5×10^{-8} mbar of isobutane, subsequently annealed to 140 K. There is no hint that isobutane sticks to the water surface.

6.4.2.3. Thermal desorption experiments of the water/isobutane system

Analogous experiments to those conducted for methane (see Section 6.4.1.3.) were also performed for isobutane. Fig. 6-7 displays the TPD spectra for 1 ML of isobutane on ASW (red curve), CI (blue curve), and Pt(111) (green curve). (TPD results involving higher isobutane coverages are documented in Supplementary materials Fig. S3.) The desorption peak temperatures of 97.1 K and 98.5 K from CI and ASW are relatively close while desorption from Pt(111) occurs much higher, peaking at 167 K. Using the method described in Section 6.4.1.3., an estimate of the binding energy was obtained using the Polanyi-Wigner equation. A prefactor of ~10^{15} s^{-1} had previously been determined experimentally for butane desorption from MgO(100), C(0001)/ Pt(111), and Pt(111) [45] and was used here as a reasonable estimate of the isobutane desorption prefactor. The estimated binding energies were 29.6, 27.9, and 50.3 kJ/mol for isobutane on ASW, CI, and Pt(111) respectively. As was the case for methane, the isobutane binding energies on ASW and CI are lower than the hydrogen bond energy of 29.5 kJ/mole in crystalline ice [46] and the multilayer sublimation energy of ~55 kJ/mol for ASW and CI [47].

Fig. 6-8 displays the TPD spectra for 1 ML of isobutane from underneath of ASW overlayers of 25, 50, 100, and 200 ML. As described in Section 6.4.1.3., the peaks from 155 to 165 K are "volcano" peaks and those above ~165 K are "trapped" peaks. The overall pattern with increasing ASW thickness is nearly identical to that observed for methane. The overall similarity of the isobutane results with those for methane (Fig. 6-4(b)) and other gases [16,17,48-50] suggests that isobutane does not uniquely change the behavior of the ASW overlayer. That is, we observe no evidence for the formation of isobutane induced clathrate structures.
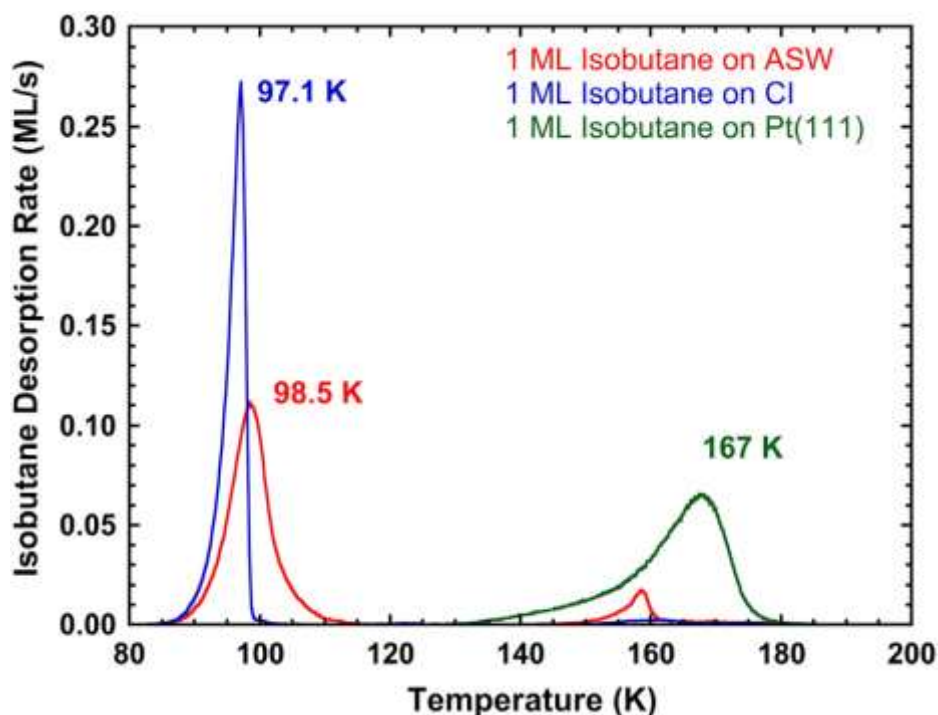

Figure 6-7. TPD spectra for 1 ML of isobutane deposited on a 100 MLthick ASW film (red curve), on a 100 ML thick crystalline ice film (blue curve), and on bare Pt(111) (green curve). Isobutane was deposited at 30 K and the heating rate was 1 K/s.
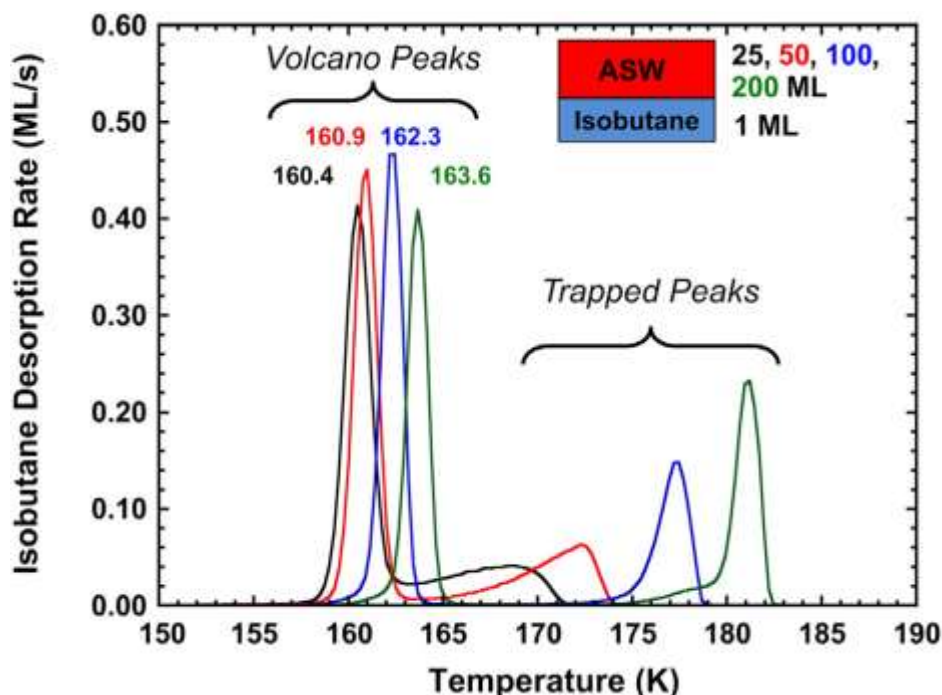
Figure 6-8. TPD spectra for 1 ML of isobutane deposited underneath of ASW thicknesses of 25 (black), 50 (red), 100 (blue), and 200 ML (green). Isobutane and water were deposited at 30 K and the heating rate was 1 K/s. The peaks between 155 and 165 K labeled as "volcano peaks" are due to isobutane desorption that occurs during ASW crystallization. The "volcano" peak shifts to higher temperature with increasing overlayer thickness. The peaks between 170 and 185 K are labeled as "trapped peaks" and are due to isobutane desorption that occurs during the desorption of the ASW overlayer.

6.5. Conclusions

Various different kinetic pathways have been explored with the goal of facilitating water-HFNG interaction and tracking the evolution of the water-HFNG samples with molecular-layer precision. At 140 K and pressures at which gas pressure and sample temperature could be well controlled in our UHV apparatus, methane and isobutane exhibit a remarkably weak interaction with water. Applying up to 0.1 mbar of methane or 10^{-5} mbar of isobutane in co-deposition experiments did not produce clathrates, and only led to ice formation. Capping a molecular layer of isobutane with two molecular layers of water might have led to substrate-induced hydrate formation, but the alternative explanation that the presence of isobutane merely facilitated dewetting and clustering of water is at least as likely. In principle, tracking methane clathrate formation with scanning probe microscopy might be possible. But keeping a sample at ~140 K and simultaneously exposing it to nearly atmospheric pressure methane would pose a serious design challenge for vibration-isolated microscopy setups: the sample has to be cooled without exposing other cold surface areas to water and the hydrate forming gas.

The TPD results support the idea that the interactions of methane and isobutane with water at the temperature and pressure (UHV) conditions of these experiments do not induce the formation of

70

clathrate structures. Based on the monolayer desorption temperatures of ~43 K for methane and ~100 K for isobutane, the estimated adsorbate-water interaction energies are weaker than the water hydrogen bond energy and the multilayer water sublimation energy. These relatively weak HFNG-water interactions lead to rapid desorption of the HFNG at low temperature, making it difficult to maintain a significant HFNG coverage on either ice or ASW at higher temperatures for the HFNG pressures attainable in typical UHV-based surface science experiments. Experiments where the two adsorbates were deposited underneath of water overlayers provided no evidence for clathrate formation. Instead the two gases displayed the familiar "volcano" and "trapped" peak behavior exhibited by many other gases. Overall, the TPD results show that the adsorbate-water interactions are weaker than the water-water interactions, which supports the interpretations of the STM results. One would expect that for any adsorbate, regardless of the interaction energy, a minimum contact time and/or a steady-state HFNG coverage at a critical temperature would be required to induce clathrate formation.

For example, it is instructive to estimate the adsorbate coverage for the pressure and temperature conditions of these experiments. The steady-state adsorbate coverage is determined by equating the adsorption and desorption fluxes, $J_{in} \times S = k_{Des} \times \theta$, where J_{in} is the incident flux, S is the sticking coefficient, k_{Des} is the temperature dependent desorption rate constant, and θ is the surface coverage. Rearranging this equation and for a sticking coefficient of 1, the steady-state coverage is given by $\theta_{SS} = J_{in} / k_{Des}$. The incident flux on the surface, J_{in}, can be calculated using the equation from gas kinetic theory, $J_{in} = P / (2\pi\, mkT)^{1/2}$, where P is the gas pressure, m is the molecular weight, k is the Boltzmann constant, and T is the gas temperature [52]. The desorption flux is given by, $J_{des} = k_{Des}\theta = v\, \theta \exp(-E / RT)$, where v is the prefactor and E is the adsorbate binding energy. Prefactors for methane and isobutene were 1×10^{13} s^{-1} and 1×10^{15} s^{-1}, respectively, and the binding energies were those obtained from the 1 ML TPD spectra described in Sections 6.4.1.3. and 6.4.2.3. The binding energies for methane on CI (11.2 kJ/mol) and for isobutane on CI (27.9 kJ/mol) were used. For the methane experimental conditions in Fig. 6-1(b,c), a background pressure of 0.10 mbar and a surface temperature of 145 K, the calculated steady-state coverage is 6.6×10^{-5} ML. For the isobutane experimental conditions in Fig. 6-5(b), a background pressure of 1.0×10^{-5} mbar and a surface temperature of 140 K, the steady state coverage is 1.5×10^{-4} ML. The extremely low steady-state coverages for the low-pressure conditions of our experiments likely account for our inability to observe clathrate formation. One expects that the probability of clathrate formation would increase with the coverage of the HFNG species. In the Introduction we mentioned the observation of clathrate formation at 9 bar for methane and 0.18 bar isobutane at 242 K. For these conditions we estimate a steady-state coverage of 0.14 ML for methane and 0.13 ML for isobutane. One can now calculate the pressure required to achieve these coverages at the temperatures of the STM experiments. To obtain a steady-state coverage of 0.14 ML for methane on CI at 145 K would require a gas pressure of 213 mbar. Similarly, to obtain a coverage of 0.13 ML of isobutane on CI at 140 K, a gas pressure of 7.6×10^{-2} mbar would be needed. Obviously, to obtain these steady-state coverages requires pressures that are well-above the pressure conditions for UHV systems.

In summary, our STM and TPD experiments show that, at low pressure, methane's and isobutane's interactions with water are extremely weak. At the lowest temperature at which the mobility of water molecules should still suffice for the assembly of clathrate cages, ~140 K, and at the highest gas pressures accessible in our UHV setup, i.e., $p_{Meth} = 0.10$ mbar and $p_{Isob} = 10^{-5}$

mbar, co-deposition of water with methane or isobutane results in pure ice formation. This observation is consistent with the very low binding energies measured with TPD for methane and isobutane ML on ice, i.e., 11 kJ/mol and ~28 kJ/mol. Apparently, steady-state surface coverages estimated from these binding energies, $\theta_{\text{Meth}} = 6.6 \times 10^{-5}$ ML and $\theta_{\text{Isob}} = 1.5 \times 10^{-4}$ ML, are too low to drive the re-arrangement of water molecules from an ice lattice into clathrate cages. STM and TPD also found no clear evidence that hydrates formed when gases and water were deposited sequentially.

Our experiments conducted at pressures < 0.1mbar and temperatures as low as 140 K (STM experiments) and < 185 K (methane and isobutane desorption) do not capture the environmental conditions under which clathrates form on Earth. Nevertheless they can serve as benchmarks against which realistic geophysical models can be tested, e.g., whether those models are able to reproduce our measured desorption energies. Though absent on Earth, the low-pressure/low temperature conditions of our experiments are present in a range of astrophysical settings where the occurrence of clathrates had been suggested, for example, in comets [5,53], on outer planets and their moons [4,6,7,54], and even the polar, permanently-shaded craters on Earth's moon [55].

6.6. Acknowledgments

6.7. Supplementary Information

Supplementary data to this article can be found online at http://dx.doi.org/10.1016/j.susc.2015.07.013.

6.8. References

[1] E.D. Sloan, C. Koh, Clathrate Hydrates of Natural Gases, third ed. CRC Press, Boca Raton, FL, 2008. (and references therein).
[2] K.A. Kvenvolden, Org. Geochem. 23 (1995) 997.
[3] A.V. Milkov, Earth Sci. Rev. 66 (2004) 183.
[4] S.L. Miller, Proc. Natl. Acad. Sci. 47 (1961) 1798.
[5] A.H. Delsemme, A. Wenger, Planet. Space Sci. 18 (1970) 709.
[6] N. Fray, U. Marboeuf, O. Brissaud, B. Schmitt, J. Chem. Eng. Data 55 (2010) 5101.

[7] J.I. Lunine, D.J. Stevenson, Astrophys. J. Suppl. Ser. 58 (1985) 493.

[8] L.A. Stern, S.H. Kirby, W.B. Durham, Science 273 (1996) 1843.

[9] L.A. Stern, S.H. Kirby, S. Circone, W.B. Durham, Am. Mineral. 89 (2004) 1162.

[10] W.F. Kuhs, D.K. Staykova, A.N. Salamatin, J. Phys. Chem. B 110 (2006) 13283.

[11] S.R. Davies, K.C. Hester, J.W. Lachance, C.A. Koh, E.D. Sloan, Chem. Eng. Sci. 64 (2009) 370.

[12] B.J. Falabella, M. Vanpee, Ind. Eng. Chem. Fundam. 13 (1974) 228.

[13] A. Falenty, G. Genov, T.C. Hansen, W.F. Kuhs, A.N. Salamatin, J. Phys. Chem. C 115 (2011) 4022.

[14] A. Falenty, A.N. Salamatin, W.F. Kuhs, J. Phys. Chem. C 117 (2013) 8443.

[15] Y.K. Kim, S.C. Park, J.H. Kim, C.W. Lee, H. Kang, J. Phys. Chem. C 112 (2008) 18104.

[16] P. Ayotte, R.S. Smith, K.P. Stevenson, Z. Dohnalek, G.A. Kimmel, B.D. Kay, J. Geophys. Res. Planets 106 (2001) 33387.

[17] R.A. May, R.S. Smith, B.D. Kay, J. Chem. Phys. 138 (2013) 104501.

[18] E.D. Sloan, F. Fleyfel, AICHE J. 37 (1991) 1281.

[19] R.T. Cygan, S. Guggenheim, A.F.K. van Groos, J. Phys. Chem. B 108 (2004) 15141.

[20] R.W. Hawtin, D. Quigley, P.M. Rodger, Phys. Chem. Chem. Phys. 10 (2008) 4853.

[21] G.J. Guo, M. Li, Y.G. Zhang, C.H. Wu, Phys. Chem. Chem. Phys. 11 (2009) 10427.

[22] B.C. Knott, V. Molinero, M.F. Doherty, B. Peters, J. Am. Chem. Soc. 134 (2012) 19544.

[23] S.A. Bagherzadeh, P. Englezos, S. Alavi, J.A. Ripmeester, J. Phys. Chem. B 116 (2012) 3188.

[24] P. Pirzadeh, P.G. Kusalik, J. Am. Chem. Soc. 135 (2013) 7278.

[25] K.A. Kvenvolden, Rev. Geophys. 31 (1993) 173.

[26] D.E. Brown, S.M. George, J. Phys. Chem. 100 (1996) 15460.

[27] S. Nie, N.C. Bartelt, K. Thürmer, Phys. Rev. Lett. 102 (2009) 136101.

[28] G.D. Holder, S.P. Godbole, AIChE J 28 (1982) 930.

[29] P.V. Hobbs, Ice Physics, Clarendon Press, Oxford, 1974.

[30] K. Thürmer, S. Nie, Proc. Natl. Acad. Sci. 110 (2013) 11757.

[31] S. Nie, P.J. Feibelman, N.C. Bartelt, K. Thürmer, Phys. Rev. Lett. 105 (2010) 026102.

[32] S. Standop, M. Morgenstern, T. Michely, C. Busse, J. Phys.-Condes. Matter 24 (2012) 124103.

[33] K. Thürmer, S. Nie, P.J. Feibelman, N.C. Bartelt, J. Chem. Phys. 141 (2014) 18C520.

[34] S. Maier, I. Stass, T. Mitsui, P.J. Feibelman, K. Thürmer, M. Salmeron, Phys. Rev. B 85 (2012) 155434.

[35] K. Thürmer, N.C. Bartelt, Phys. Rev. B 77 (2008) 195425.

[36] K. Thürmer, N.C. Bartelt, Phys. Rev. Lett. 100 (2008) 186101.

[37] R.S. Smith, T. Zubkov, B.D. Kay, J. Chem. Phys. 124 (2006) 114710.

[38] T. Zubkov, R.S. Smith, T.R. Engstrom, B.D. Kay, J. Chem. Phys. 127 (2007) 184707.

[39] G.A. Kimmel, K.P. Stevenson, Z. Dohnalek, R.S. Smith, B.D. Kay, J. Chem. Phys. 114 (2001) 5284.

[40] G. Zimbitas, S. Haq, A. Hodgson, J. Chem. Phys. 123 (2005) 174701.

[41] G.A. Kimmel, N.G. Petrik, Z. Dohnalek, B.D. Kay, Phys. Rev. Lett. 95 (2005) 166102.

[42] S. Nie, N.C. Bartelt, K. Thürmer, Phys. Rev. B 84 (2011) 035420.

[43] G.A. Kimmel, N.G. Petrik, Z. Dohnalek, B.D. Kay, J. Chem. Phys. 126 (2007) 114702.

[44] A.M. Dejong, J.W. Niemantsverdriet, Surf. Sci. 233 (1990) 355.

[45] S.L. Tait, Z. Dohnalek, C.T. Campbell, B.D. Kay, J. Chem. Phys. 125 (2006) 234308.

[46] V.F. Petrenko, R.W.Whitworth, Physics of Ice, Oxford University Press, Oxford; New York, 1999.

[47] R.S. Smith, J. Matthiesen, J. Knox, B.D. Kay, J. Phys. Chem. A 115 (2011) 5908.

[48] R.S. Smith, C. Huang, E.K.L. Wong, B.D. Kay, Phys. Rev. Lett. 79 (1997) 909.

[49] R.A. May, R.S. Smith, B.D. Kay, J. Phys. Chem. Lett. 3 (2012) 327.

[50] R.A. May, R.S. Smith, B.D. Kay, J. Chem. Phys. 138 (2013) 104502.

[51] C. Xu, B.E. Koel, M.T. Paffett, Langmuir 10 (1994) 166.

[52] G.A. Somorjai, Introduction to Surface Chemistry and Catalysis, Wiley, New York, 1994.

[53] U. Marboeuf, O. Mousis, J.M. Petit, B. Schmitt, Astrophys. J. 708 (2010) 812.

[54] E. Lellouch, B. Bezard, F.M. Flasar, S. Vinatier, R. Achterberg, C.A. Nixon, G.L. Bjoraker, N. Gorius, Icarus 231 (2014) 323.

[55] N.S. Duxbury, K.H. Nealson, V.E. Romanovsky, J. Geophys. Research-Planets 106 (2001) 27811.

DISTRIBUTION

4   Pacific Northwest National Laboratory
    Attn: B. D. Kay (1)
           G. A. Kimmel (1)
           R. S. Smith (1)
           C. Yuan (1)
    P.O. Box 999, MSIN K8-88
    Richland, WA 99352

1	MS0701	P. B. Davies	6900
1	MS0706	D. J. Borns	6912
2	MS0734	M. E. Gordon	6124
1	MS0734	A. Martino	6124
1	MS0735	E. K. Webb	6910
8	MS0754	R. T. Cygan	6910
1	MS0754	S. J. Altman	6915
1	MS0754	D. B. Hart	6915
1	MS0754	J. A. Greathouse	6915
1	MS0754	R. C. Moore	6915
2	MS0754	S. L. Teich-McGoldrick	6915
1	MS1411	S. P. Meserole	1816
1	MS1411	M. A. Rodriguez	1819
1	MS9001	M. C. Walck	8000
2	MS9161	K. Thürmer	8342
1	MS0899	Technical Library	9536 (electronic copy)
1	MS0359	D. Chavez, LDRD Office	1911